2018

Regolith-Based Construction Materials for Lunar and Martian Colonies

Kevin Grossman
University of Central Florida

REGOLITH-BASED CONSTRUCTION MATERIALS FOR LUNAR AND MARTIAN COLONIES.

by

KEVIN GROSSMAN
Bachelor of Science, SUNY, The College at Brockport, Brockport, NY 2012
Master of Science and Engineering, University of Central Florida, Orlando, FL, 2015

A dissertation submitted in partial fulfillment of the requirements
for the degree of Doctor of Philosophy
in the Department of Material Science and Engineering
in the College of Engineering and Computer Science
at the University of Central Florida
Orlando, Florida

Fall Term
2018

Major Professor: Sudipta Seal

ABSTRACT

Humankind's ambitions of exploring our solar system and parts beyond depend heavily on our ability to collect resources from local environments at our destinations rather than bringing materials on the journey. This is a concept known as in-situ resource utilization (ISRU) and it is one that has been understood by every explorer and settler in the history of humankind. Regolith on the moon and Mars has been shown to be a particularly useful resource and has the ability to provide humans with resources including water, oxygen, construction material, fabric, radiation shielding, metals, and may more. This dissertation focuses on construction materials derived from standard regolith simulant JSC-1A, including bricks, composites, metals and modified powder materials. Sintering processes with JSC-1A were studied to determine optimal heating profiles and resulting compressive strengths. It was determined that the temperature profiles have an optimal effect on smaller particle sizes due to the larger surface area to volume ratio of small particles and sintering being a surface event. Compressive strengths of sintered regolith samples were found to be as high as 38,000 psi, which offers large utility for martian or lunar colonies.

This study also investigates a method for extracting metals from regolith known as molten regolith electrolysis. The alloy of the two major metallic components of regolith, iron and silicon, has been investigated as a structural metal for colonies and a potential feedstock for novel metallic 3D printers. Parallel to these efforts, a new additive manufacturing technique designed to print metal parts in low and zero gravity environments is developed. The mechanical properties from metal parts from this technique are examined and it is determined how the printing process determines a microstructure within the steel that impacts the utility of the technology.

I would like to thank my parents for their unending support.

ACKNOWLEDGMENTS

I would like to thank my faculty advisor, Prof. Sudipta Seal, for his support and motivation during my course of study and research at UCF. I am thankful to the thesis committee members for (Dr. Lei Zhai, Stephen Floreczk, Michael Leuenberger and Dr. Jiyu Fang) for providing their valuable time, as well as my fellow researchers at the Advanced Materials Processing and Analysis Center (AMPAC), who have always been willing to lend a helping hand to me. This research has been funded by AMPAC and NASA with help from RDO induction Inc, Made in Space Inc. I would also like to thank Abhishek Mehta for his help.

TABLE OF CONTENTS

LIST OF FIGURES

LIST OF TABLES

CHAPTER ONE: INTRODUCTION

Maslow's hierarchy of needs describes the requirements for humans to live a happy and fulfilled life. If we hope to put humans on Mars, the moon or any other planet for an extended period of time, we must be able to satisfy the needs of Maslow's hierarchy in the most hostile of environments. At the base of the hierarchy is the most material needs; food, water, oxygen, and shelter (safety). The purpose of in-situ resource utilization (ISRU) is to harvest these vital resources from local environments of the moon or Mars. This approach to colonization has two advantages: it eliminates the need for a continuous train of resupply missions to the colony and it allows for a drastic minimization of the payload weight of manned missions. The cost of putting materials into low earth orbit (LEO) is estimated to be as high as $10k per kilogram of payload [1]. Recent advancements in the field, such as reusable rockets by SpaceX and Blue Origin have cut down this cost by as much as 30% [2]. Despite these major advancements, the cost of launching rockets is still a prohibitive factor for space exploration beyond LEO. NASA has plans to send humans to Mars by the 2030's [3] and SpaceX has made similar claims [4] with a purpose of building permanent settlements on another planet and transforming humanity into a multi-planetary civilization. Very large payloads sitting atop very large rockets are being imagined to carry the crew and all necessary materials for the mission [5]. Despite the ability to make such large rockets, minimizing payloads to include only what is necessary is an imperative aspect for mission success and scientists believe the key to achieving this is in-situ resource utilization or "on-site resource utilization". Living off the land as a means of obtaining all consumable

materials is the only way space exploration and colonization is a possibility.

1.1 In-Situ Resource Utilization

ISRU technologies include locating, harvesting and processing resources from the local environment or from materials that would otherwise be considered waste to colonists. Locating and mapping resources is already underway with mars orbiters and the mars science laboratory rover collecting data on Martian soils and atmospheric conditions [6,7]. Mars and the moon seemingly have very little resources to offer humans, but what they both have in common is a layer of crushed rock, known as "regolith", covering the surface down to a depth of several meters. Martian and lunar regolith is composed largely of metal oxide materials that have been crushed into a fine powder from billions of years of high-energy impact events from asteroids. Along with providing sufficient energy to crush the surface rocks into powder, asteroid impacts also introduce varieties of elements into the local soil, making the exact composition of lunar and Martian soil a function of location [8-10].

Mars also has a gaseous atmosphere to that can be utilized. While the moon's atmospheric pressure is essentially negligible, Mars' atmosphere has a pressure 1% that of Earth and is nearly entirely CO_2 [11] which can be converted into several resources including breathable oxygen [12], methane for propellant [13] and simple polymers such as polyethylene [14]. The moon and Mars also offer severe temperatures and an essential vacuum as resources available to its habitants. In-situ resource utilization is a crucial category of technologies for the hopes of a long-term human presence in space and, more specifically, on Mars or the moon. The

idea of living off the land is not a new concept and has been understood by every explorer and settler in the history of the world. Harvesting materials from the local environment on the moon or Mars instead of transporting them from Earth will save an enormous amount of money and reduce the weight of a launch vehicle drastically, making colonization possible.

Water is one of the most vital resources and has been the driving force in a large amount of the exploration of our solar system. Wherever there is a chance of finding water, NASA has dedicated more and more money toward exploring that location. On Mars, there is very little water suspended in the atmosphere but large amounts of frozen water on the polar caps of Mars and even larger deposits of water underneath the surface, even at locations closer to the equator. These water deposits could even be liquid "oceans" underneath the surface, hidden from the low atmospheric pressure and radiation that would otherwise evaporate water [15,16]. Estimates of these underground deposits of water suggest the water-rich areas of regolith start at a minimum of 1meter deep below the surface. This estimate is driving current excavation technologies developed at NASA [17]. The regolith itself is known to contain water molecules in the form of hydrated minerals. Current measurements claim the amount of water in the regolith is between 3 and 8 wt% at the equator and as high as 40 wt% at latitudes of 60 degrees or higher. On the moon, the prospect of finding lush deposits of water has become much more likely with a recent finding that the lunar poles have large deposits of water ice in areas that never see sunlight [18]. Water on the moon may also exist in the form of hydrated minerals in the regolith.. Besides being a source for the water itself, electrolysis of the water would produce gaseous H_2 and O_2, which serve many purposes. Oxygen can be used for breathing or as an oxidizer in propellants, while the gaseous hydrogen is useful for producing methane, plastics, or being

reverted into water when combined with CO_2. These chemical processes will be discussed further later on.

Given the importance of oxygen and water for sustaining life, it is not ideal to sacrifice one resource to produce another, especially given the finite amount of water that can be found on the moon or Mars. For this reason, a large amount of effort is being dedicated to manufacture oxygen from other available resources. Atomic oxygen is nearly everywhere on both the moon and Mars, but a large amount of processing will be necessary to make use of it. Oxygen is in the atmosphere in the form of CO_2 and in the ground in the form of oxidized metals. While the moon has effectively no atmosphere, the regolith contains as much as 40 wt% oxygen atoms. This makes obtaining gaseous oxygen a mere matter of developing a technology to remove the oxygen from the oxidized metal. The leading candidate for this goal is molten regolith electrolysis, which will be discussed in a later section.

Other resources available for collection and processing include carbon, which is present in the atmosphere of Mars in the form of carbon dioxide but not on the moon, inert gasses such as argon and nitrogen are present and can be separated and refined for research or processing techniques, which require inert atmospheres. The regolith, besides containing water, consists of minerals and clays that can be useful for a variety of applications [19].

Identification, location and collection of natural resources like carbon dioxide and regolith is the first of many steps toward obtaining life-supporting resources on the moon or Mars. While technologies like RASSOR, the Mars orbiter and resource prospecting devices are an integral part of ISRU, the heart of the ISRU process is the transformation of raw materials into viable resources with the final stage of the ISRU template being the storage and utilization

of the newly minted resources. Converting CO_2 into O_2 is a chemical process with no easy method to achieve. The double bonds between oxygen and carbon atoms in the molecule make it difficult and energy intensive to separate more than one oxygen atom from the molecule, which would leave you with atomic oxygen and carbon monoxide. Collecting liquid or solid water and transporting it to a colony is the mere first step. Purifying, processing and storing the material is where impactful new ISRU technologies are being developed.

The conversion of CO_2 into useful materials is an exciting proposition considering the abundancy of carbon dioxide on Mars. The Sabatier reaction is one that produces methane, water and energy from carbon dioxide and molecular hydrogen. This reaction is written as

$$CO_2 + 4H_2 \rightarrow CH_4 + 2H_2O + energy$$

Since this reaction is exothermic, it will occur spontaneously when the reactants come into contact in the presence of a nickel or ruthenium catalyst. The most attractive product of this reaction is the methane, which can be used as a fuel for rocketry while the water product can close the loop by replenishing some of the water used to make hydrogen. Development of compact, highly efficient Sabatier reactors for in-space use is being done at Marshall Space Flight Center (MSFC) in partnership with private entities [20]. Current technologies for this reactor make use of a Microlith catalytic mesh with high surface area and heat flow which accelerates the reaction kinetics and increase CO_2 selectivity in the reaction, further increasing efficiency. This reactor is said to support a crew of up to four people on a 14 mL reactor volume. Durability and longevity tests were performed and saw no degradation of catalyst performance after 100 hours of use.

The carbon dioxide in the Martian atmosphere can also serve as a building block for

plastics and polymers, which enable many beneficial capabilities to a Martian colony. By implementing a reverse water-gas shift (RWGS) reaction, we can convert CO_2 into CO. This reaction is typically defined as:

$$H_2 + CO_2 \rightarrow H_2O + CO$$

However, by modifying the input ratio of hydrogen and carbon dioxide, the reaction can produce carbon monoxide along with hydrogen gas:

$$6H_2 + 2CO_2 \rightarrow 2H_2O + 2CO + 4H_2$$

This endothermic reaction produces water as a by-product, which can be re-cycled back into a colony's water supply while the carbon monoxide and hydrogen gas can be diverted to a second reactor where, in the presence of an iron catalyst, ethylene can be produced;

$$2CO + 4H_2 \rightarrow C_2H_4 + 2H_2O$$

This reaction to produce ethylene is exothermic, and produced enough heat energy to sustain reaction [CO production], making this process a nearly zero-input ethylene production capability. This reaction also has a large equilibrium constant, making high purity products much simpler to produce. The ethylene product of this process is a very simple monomer and can be used to produce polyethylene, more complex monomers and a variety of polymers, or can be used as a fuel source. On Earth in the past several decades, Ethylene has been a major candidate to replace conventional gasoline in automobiles. On Mars, without the availability of petroleum deposits in the ground, ethylene may be the only option to fuel machinery based on engines similar to a combustion engine.

1.2 Regolith Simulants

In recent decades, simulated regolith powders have been developed to be used as a platform for studying granular mechanics in space, develop robotic systems for regolith operations and to enable research on the chemistry and bio-habitability of Martian and lunar dirt. One of the most prevalent simulants, JSC-1A (named for Johnson Space Center) was developed as a lunar simulant and has been certified by NASA to be mechanically and chemically similar to the lunar return samples from the Apollo missions. Figure shows JSC particles, which are jagged and irregularly shaped. Figure 1 shows an SEM image of JSC-1A regolith.

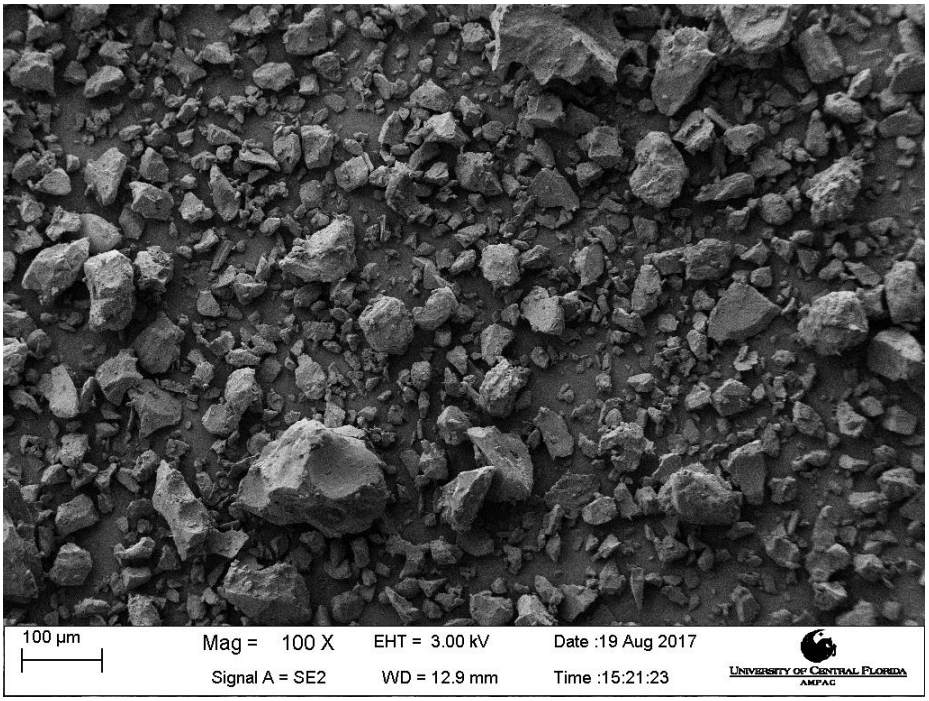

Figure 1: SEM image of unseived JSC-1A. This regolith simulant I widely used in lunar granular mechanics research due to its strong morphological and chemical resemblance to lunar dirt.

This small characteristic of lunar regolith translates into large problems when designing machinery to excavate or manipulate bulk regolith. The angle of repose and penetration strength [21] of lunar and Martian regolith is extremely high and combined with the low gravity of the moon or Mars will make any process involving pouring the material Simulants are currently being developed to enable development of operation technologies on a variety of rocky bodies including Mars and asteroids. University of Central Florida professors Dr. Dan Britt and Dr. Phil Metzger have been spearheading the effort to develop and analyze new simulants and develop a universal grading system for regolith. The quality of a simulant depends on several factors including chemical composition, particle size and morphology, presence of volatiles like water, cohesiveness, density, and many others [22].

Simulant design and production has grown recently as interest in a space-based economy has started to develop. Companies like Deep Space Industries have begun producing specialized simulants for the purpose of researching mining and resource extraction technologies for asteroid, lunar and Martian environments. Mechanical simulants like BP-1 are used for their mechanical properties where the chemical makeup of the powder is not important [23]. Processes like robotic excavation, transportation and studies on granular mechanics require only a morphological similarity to regolith.

The most obvious use for regolith is for construction material; however, its utility branches out into many unexpected areas. Recent studies have proven regolith to be an excellent thermal ablative and is being considered as an in-situ heat shield material for landers going into Martian or terrestrial atmosphere [24]. Currently, any manned capsule launched into space carries a heat shield to isolate humans and equipment from the high temperatures experienced

as a result of the large atmospheric resistance during re-entry. Carrying the heat shield into space despite only using at the end of the mission puts large requirements on the size of the launch vehicle due to the inherently large weight of the shield. The regolith-derived heat shield fits into the architecture of space colonization as a device that can be manufactured on Demos or Phobos where no heat shield is required for entry and the fuel requirements for launching are minimal due to the small gravitational field. Using regolith found on smaller bodies to construct heat shields for landing pods simplifies the process of transporting people or equipment to and from other planets by eliminating the requirement to launch such a heavy object from the larger gravitational fields of Mars or Earth. This, in turn, saves resources and enables faster colonization of other planets.

Another potential use of regolith is as a radiation shield for colonists in an environment which otherwise offers little protection from the various radiation dangers found in the depths of space [25]. Radiation is a blanket term used for high-energy emissions that pose threats to humans. On Earth, we experience low energy radiations in the form of radio waves, x-rays, microwave radiation, and even small amounts of nuclear radiation, which are generated on earth and are generally harmless if experienced in small doses. The magnetic field of the Earth, caused by the moving molten core of the earth, protects use from the many high-energy radiation events that would otherwise be bombarding the planet every day. Alpha-radiation, which is a He^{+2} atom, are the ejecta of solar events are very high energy and thus dangerous if experienced directly. However, the magnetic field of the Earth deflects these particles and protects us on the ground. The same can be said for energy cosmic radiation, which, unlike the alpha particle, is not matter but rather an electromagnetic form of radiation that can also cause great harm. On

Mars, no such magnetic field exists to protect us from these forms of radiation. Ideas of creating an artificial magnetic field around a colony are being explored [26] but such a solution would be energy intensive and therefore consume an undesirable amount of precious electricity. While not a perfect solution either, studies are being done on the effectiveness of regolith as a barrier for radiation propagation. It is hypothesized that the high iron content in typical lunar or Martian regolith would act as a significant barrier for the particle forms of radiation that would hit the colonists. The effectiveness of pure regolith as a barrier against electromagnetic radiation has not been studied although it is believed metals would act as a better shield for those forms of radiation.

Although the goal of using regolith as the sole component of a construction material is a very attractive proposition, alternative routes are currently being developed as a means to bind powder regolith into a viable construction material. One such method is the addition of magnesium powders dispersed into a regolith powder to enable a thermite reaction powerful enough to flash-sinter the regolith into bricks [27]. This method boasts rapid production while relying on magnesium metal as a consumable material in the process. Another method, which offers a lot of promise in the world of automated construction, is the combination of regolith with thermoplastics similar to those used in 3D printers. Using a low melting point plastic as a binder, you can conform regolith powder into a solid piece without any physical manipulation of the regolith, which cuts down costs and time as well as offers a segway into automated construction and additive manufacturing using this material [28].

1.3 Molten Regolith Electrolysis

The process of molten regolith electrolysis (MRE) has been studied in recent years as a way of producing oxygen and metals from regolith. Electrolyzing the ceramic regolith powder into oxygen and metals provides two very important materials from an essentially unlimited source. The economic impact of a system of oxygen production on the moon or Mars cannot be overstated. Studies on the cost-per-kilogram to produce oxygen outside of Earth's gravitational well began in 1985 with a study done by the General Dynamics Space Systems Division [29]. This study determined that oxygen could be produced on the lunar surface and delivered to LEO with a price tag of $5,300 per kilogram. This cost is 1/3 that of producing oxygen on Earth and delivering it to LEO via the space shuttle. Other studies in the 90's estimate the cost of lunar-based oxygen production to be anywhere between $8,000 [30] and $18,000 [31]. The discrepancy in these studies are largely due to initial assumptions made by the researchers. Sherwood and Woodcock assumed the necessity for human operation of machinery, which is not necessarily true. However, even the most conservative estimates for the cost of lunar oxygen production are much lower than the estimated cost of delivering oxygen to the moon from Earth, which sits at $110,000/kg from a study in 2005 by the Colorado School of Mines [32]. In 1993 a study by Johnson Space Center named LUNOX (LUNar OXygen) estimated the incorporating a system for oxygen production on a lunar settlement reduced the total cost of colonization by 20% and the cost of launch vehicles by 50% [33]. While these studies show a dramatic advantage in production of oxygen on the moon, the economic and technological assumptions are out of date and these studies can be updated. However, the economic impact of oxygen production will be exaggerated even further when considering oxygen production on Mars.

Prior to electrolysis, melting the regolith at a temperature higher than 1250°C is necessary ensure mobility of ions. Shreiner et al calculated the optimal size and shape of an MRE reactor based on the concept of a "cold walled" reactor, which features a molten pool of regolith between two electrodes, and a transition into frozen regolith some distance away from the electrodes. This ensures the walls of the reactor never touch melted regolith, which is extremely corrosive and limits the lifespan of a reactor to mere hours. Studies have been done on the appropriate electrode material, which requires an electrically conductive material with enough mechanical strength to remain robust at extreme temperatures and corrosion resistance to withstand the corrosive environment of molten iron. Platinum and iridium were among the top candidates from that study [34]. As the voltage between electrodes increases, iron and silicon are among the first to be electrolyzed into metals [35]. The metal materials will collect on the anode at the bottom of the reactor, while the gaseous oxygen will be allowed to bubble to the top of the reactor and extracted through a system of hoses. Considerations for the behavior of gasses at these extreme temperatures need to be made while designing this part of the reactor. After electrolysis, the metal can be extracted either through a spicket device at the bottom of the reactor, or a refractory tube and vacuum-assisted counter-gravity extraction similar to those seen in metal manufacturing processes.

Iron and silicon being the first materials to electrolyze from their respective oxide states is coincidental and extremely useful. Since iron and silicon are typically the most prevalent materials in regolith and are very useful in their own, the production of these metals is an extremely attractive prospect. While the two metals require different applied voltages to electrolyze, the reduction process will happen coincidentally due to changing resistivities with a

dynamic molten pool composition as well as the resistance of iron to electrolyze due to induced Eddie currents and multiple oxidation states [36].

While pure iron and pure silicon will be technologically useful as resources on another planet, without further processing, the MRE process will produce the alloy of iron and silicon; FeSi, or ferrosilicon for generic composition. Ferrosilicon has previously been thought of as having limited uses and is largely only used as a deoxifier in the steel making industry. The composition related to this application is usually in the range of 50 to 75 wt% Si. Little is known about the properties of ferrosilicon outside of this composition range. This dissertation involves the production of novel ferrosilicon compositions and studying their properties for structural and electrical applications as a metal that can be mass-produced in space. While carbon is possible to obtain on Mars through the reduction of carbon dioxide into oxygen and carbon, this process is difficult and energy intensive. Therefore, alternative alloys

Though simple in principle, the reaction must occur at a temperature at which the ceramic regolith material is molten to allow for the movement of newly formed ions toward their respective electrodes. This creates a problem for reactor material design since a sustained operation at temperatures in excess of 1600°C is a challenge in its own without the added complexity of a molten iron species being extremely corrosive to ceramic materials [37]. Advances in electrode material have been made but are still hindered by the extremely corrosive conditions at high temperatures, but the inside walls of a reactor remain vulnerable. The solution proposed by Sirk et al [37] to this corrosion is a cold-walled reactor design in which the pool of molten regolith is heated from the inside and the portion directly between the electrodes is molten while the regolith in contact with the inner walls of the reactor remain frozen, preventing any

contact with corrosive agents. In order to achieve this cold-walled reactor design, a system for heating exclusively the center of a regolith bed beyond its melting point must be developed and a circuit for maintaining joule-heating of the molten regolith must be built into the electrodes. Joule-heating relies on the electrical resistivity of the molten pool to produce heat from an electrical current. Once melted, the regolith can rely on joule-heating to sustain its temperature [38]. The material selection for the reactor electrodes are also a subject of ongoing research. At high temperatures, with demanding electrical and mechanical requirements along with the need to withstand extremely corrosive environments from the molten metals as well as the produced oxygen, most metallic materials fail in one of the above areas. The leading candidates for cathode materials are the platinum group metals, which have been studied in extreme environments to varying degrees of success [39].

Despite the many technical challenges this poses, the MRE reactor promises extremely high rewards for its successful development and operation. The oxygen evolved during the MRE process can be easily used in breathable air for colonists as well as an oxidizer for propellant in launch vehicles. The metal products of MRE are the focus of this study and offer a promising feedstock material for in-space manufacturing, particularly for wire-based 3D metal printing. The metals produced from MRE depend on the composition of the regolith used, however most rocky bodies contain iron and silicon as their primary constituents. Of the metals typically present on regolith found on the moon or Mars, iron and silicon have the lowest reduction potentials (0.447 V and 0.857 V respectively) and therefore are the first metals to be reduced in the MRE reactor [40]. This makes iron and silicon, particularly the alloy of the two, an attractive area of focus for applications on Mars or the moon. Plans to colonize the moon or Mars depend heavily on

automated construction and manufacturing and development in 3D printing and additive manufacturing has grown significantly in the last decade. Metal 3D printers still largely utilize the powder bed system, which makes them near impossible to implement in space or low gravity environments. Wire-fed metal 3D printers offer a much better alternative for manufacturing parts and structures on lunar or Martian colonies. For this reason, we are examining the utility of the ferrosilicon product of the MRE reactor for use as a feedstock material for a wire-based metal printer. This dissertation describes several studies on the utility of metals that can be derived from the MRE process. While the current state of the MRE reactor has not yet successfully electrolyzed regolith simulant into metals, the products of the process have been predicted in previous studies. To prove the utility of the metal products of MRE in off-world applications, simulated versions of these metals have been synthesized and studied in this dissertation. The MRE process involves several key systems that have not been developed and are the subject of ongoing investigations. Parallel to those efforts, this dissertation is intended to prove the advantages of the MRE reactor and justify the development of such a system that can enable very important technologies for off-world applications.

CHAPTER TWO: SINTERING AND BINDING PROCESSES FOR REGOLITH BRICK CONSTRUCTION

In-situ resource utilization (ISRU) has become an area of intense focus as more and more energy is being applied to colonizing the moon or Mars. ISRU is the concept of relying on local resources at the destination for consumable materials rather than bringing materials from Earth. The cost of rocketry is heavily based on weight and sending a large rocket like the Space Launch System (SLS) to the moon or Mars will cost an enormous amount of money. It is therefore imperative to reduce the total vehicle mass and one of the major key in doing so is investing research into ISRU technologies that will minimize launch mass requirements as well as allow for a fully self-sustaining colony on another surface.

One of the most abundant resources on the moon or Mars is the layer of fine powders of rocky material known as regolith. The top layer of regolith, thought of as lunar soil, is almost entirely metal oxide material and is the result of billions of years of asteroid impacts and a lack of volcanic or tectonic activity to re-circulate and refresh the surface layer [41]. The exact composition of lunar regolith varies from location to location since every asteroid impact introduces foreign materials to the surface layer [42-44]. A general formula for the composition has been studied from the Apollo mission return samples and a simulated version of lunar regolith called JSC-1A, was developed at Johnson Space Center (JSC) and mass-produced for scientific research. The simulant is considered chemically and physically similar to lunar regolith and is widely used for lunar ISRU research. The composition of this simulant, like that of the moon, is largely silicates with alumina and iron oxide being the 2nd and 3rd largest constituent respectively

with other metal oxides such as MgO, CaO each making up less than 10 wt% of the total simulant [45]. Technologies for compacting regolith powder into solidified material are being developed for construction materials and each process has benefits and drawbacks. Most of these technologies involve embedding the regolith powder into a binder of either polymer or ice. These can work under certain circumstances but requires the synthesis of polymers, which is nearly impossible on the moon and difficult on Mars. Embedding regolith in ice to form construction material unnecessarily uses up one of our most precious resources and limits our colonization zone to wherever the surface is unable to reach temperatures above the freezing point of water. A better alternative is to sinter the metal oxide material into a solid by heating it to a temperature below the melting point and allowing the surfaces of particles to diffuse into each other [46-48]. This forms a solid piece of regolith while avoiding the corrosivity and energy requirements of melting regolith and eliminates the need for additives or any additional processing of materials.

Sintering occurs when metal or ceramic materials are heated to a point where solid-state diffusion is enabled. It is thermodynamically driven to reduce the overall surface area of two or more particles by coalescing them. However, as surface area decreases, new interfaces between grains emerge which has a thermodynamic cost associated with it. Mathematically, this relationship is represented with an equation for the Gibb's free energy of the system [49].

$$\delta G_{sys} = \delta \int \gamma_S dA_S + \delta \int \gamma_I dA_I$$

Where $\gamma_S dA_S$ is the infinitesimal change in surface energy as the total surface area changes and $\gamma_I dA_I$ is the energy associated with creating a new interface between the grains of separate particles. This balance of competing forces determines the sintering behavior of granular

materials.

Development and production of simulants has become a major area of research lately, with a growing "space economy" on the horizon. Simulants made to mimic various rocky bodies such as Mars, the moon, and even asteroids are being developed for different applications. Simulants can be used to mimic mechanical properties, chemical properties or both. At the University of Central Florida, Dr. Dan Britt has developed a new Martian simulant, named "Martian Global Simulant" (MGS-1) designed to mimic the mineralogical and mechanical properties of Mars based on the average chemical composition. The properties of the powdered simulant have been studied, however this novel simulant has never been sintered into bricks for mechanical studies.

Previous studies on sintering regolith have focused on unfiltered JSC-1A, which can range in particle size from those in the nano-regime up to particles as large as half a millimeter [50-52]. Sintering material with this broad size range can lead to several problems. Smaller particles tend to settle toward the bottom of a mold during compaction or any movement or vibration, which causes a stratification of particle sizes within the sintered sample. The other problem is an uneven sintering of adjacent particles. Since sintering is a surface event and smaller particles have a higher mass percentage in their surface, larger particles will not sinter to the same degree as smaller particles given the same heating conditions. Relatively un-sintered particles embedded in a matrix of well-sintered material will behave as stress concentrators in compression and result in a lower compressive strength material. Hence, in this study, we have sieved JSC-1A into narrow range size categories for a sintering study. We have compared the sintering characteristics and compressive strength of JSC-1A bricks from varied starting particle sizes and shown the ability to produce a nearly fully compacted material with extremely high compressive strength.

This process of creating materials lends itself easily to production of construction material on the moon or eventually Mars since only a source of heat is needed and the actual material can be found anywhere on the surface.

2.1 Methods of Sintering Regolith

For this study, lunar regolith simulant JSC-1A and Martian simulant MGS-1, were sieved into groups of particle size ranges. The full JSC-1A simulant, shown in figure 1, has particles ranging from the nano regime up to granules as large as half a millimeter or larger with the majority of the mass of the simulant in the range of 100 to 250 µm. Much of the research in this area has focused on solidifying the entire range of particles in the lunar simulant. This approach can cause problems with the final product for two reasons. First, the powder can stratify in a mold if shaken or compacted prior to sintering which will result in an uneven product. Second, the low surface area to volume ratio of the larger particles makes the sintering process much slower in that size range compared to the smaller particles. Since there will be an uneven sintering of particles, there exists a strong possibility for a large, mostly unsintered regolith particle to be embedded in a matrix of well sintered material. That would make the large particle effectively a defect in the brick and act as a stress concentrator, lowering the compressive strength of the overall brick.

To avoid large pores and ensure proper densification of sintered regolith, the largest size ranges of regolith will be removed from this study. The remaining simulant powder will be separated into the following size ranges: <45 µm, 45 to 90 µm, 90-180 µm and 180-280 µm. The

powder samples of each size range will be poured into the molds incrementally while being compacted vibrationally to minimize voids in the final product. Vibrational compaction also causes a stratification of powders based on particle size. For this reason, the size ranges were chosen so that the maximum size was no more than twice the minimum size. This ranging scheme produces a narrower size range as particle size decreases which is important due to the increasing surface area-to-volume ratio with decreasing particle size. Due to the stratification effect of the vibrational compaction, sintered samples of full, unseived JSC-1A or MGS-1, where the particle size range is very large, were not studied. As a control for the effect of vibrational compaction, a set of samples of each particle size was sintered without the vibrational compaction. All samples were sintered in cylindrical silica molds to produce compressive strength test coupons with a 2:1 height to diameter ratio. The heating profile for each sample followed a template of a 2 hour ramp from room temperature up to the maximum temperature, held at the maximum temperature for a given amount of time (30 minutes to an hour) and allowed to furnace cool back to room temperature prior to removal and post-processing. Sintering temperatures of 1150°C and 1200°C were chosen as the low and high temperature options. Sintering trials of temperatures higher than 1200°C resulted in melted the regolith, which became very corrosive and broke through the alumina mold. The molten regolith also solidified into a black glass that was extremely brittle. Figure 2 shows images of this glass. Post-sintering machining was done on sintered samples to ensure even, parallel surfaces and uniform diameter of the coupons. Full characterization of the powder as well as sintered product includes particle size measurements, destructive compressive strength measurements followed by SEM imaging, EDX and BET. SEM imaging was done to determine the degree of densification. Porosity measurements were taken using a water saturation

technique described by Cui and Chen [53, 54]. It is hypothesized that the lowest particle size ranges will produce the highest compressive strength results due to a higher surface area-to-volume ratio, leading to higher mobility of atoms and a higher degree of sintering and densification.

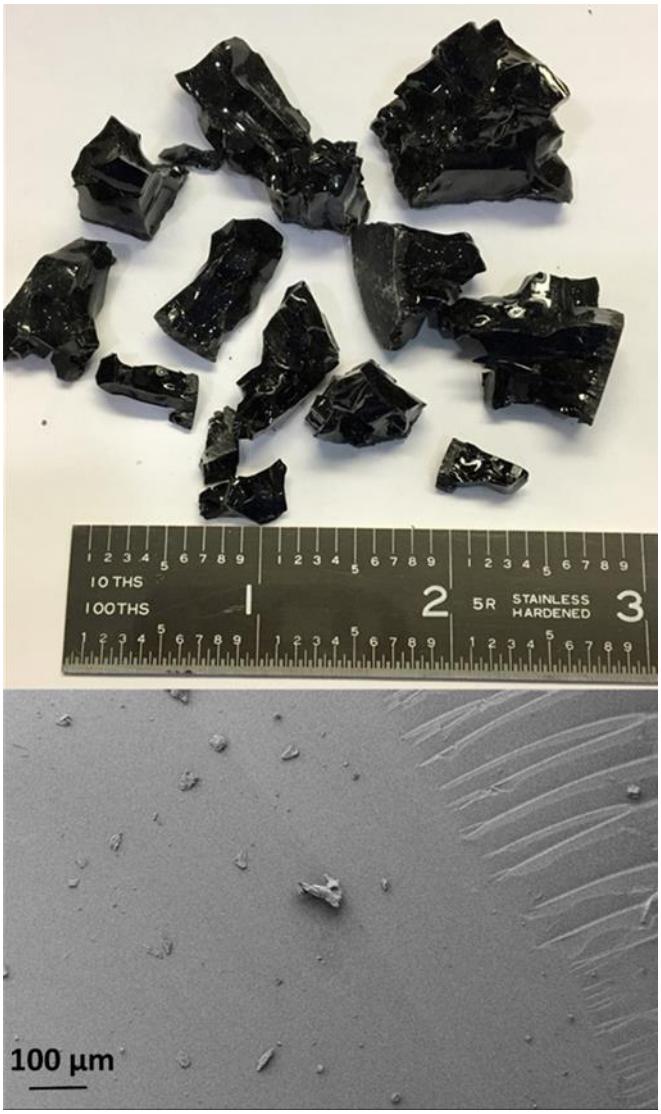

Figure 2: (Top) image of regolith shards after melting above 1220°C and (Bottom) SEM image of surface showing complete densification and smooth surface of glassy substance. The material is

very brittle and was therefore excluded from mechanical testing for this study.

The categories of particle sizes were examined prior to sintering using a MicroTrac PartAn Mini fine particle analyzer. Alumina molds were made from Cotronics Rescor castable ceramic (part no. 780) material and sintering was done in a Deltech bottom loaded resistive furnace. SEM imagine was done using a Zeiss ULTRA-55 FEG SEM. The X-ray diffraction (XRD) pattern was recorded by a PANalytical Empyrean #1 diffractometer using CuKα radiation (λ =1.54056 Å) in the range of $10° \leq 2\theta \leq 80°$ at 40 keV.

2.1.1 Characterization of Sintered Regolith

The particle size distribution for each sample is shown in figure 3. The minimum and maximum particle sizes were chosen such that no particle is more than twice the radius of the smallest particle. Since sintering is a surface phenomenon, it is important to keep the surface area for particles in a given sample relatively similar. Our analysis shows sieving the samples three times was sufficient for our purposes and that over 90% of the particles fit within the targeted size range. SEM images of the sieved particles is shown in figure 4. The JSC-1A simulant has very uniform, smooth particles while MGS-1 has extremely irregularly shaped particles and many particles with rough surface texture. This likely has an impact on the packing phenomonen occurring during the vibrational compaction prior to sintering. With rough surfaces, there was likely less surface contact for the sintering to occur.

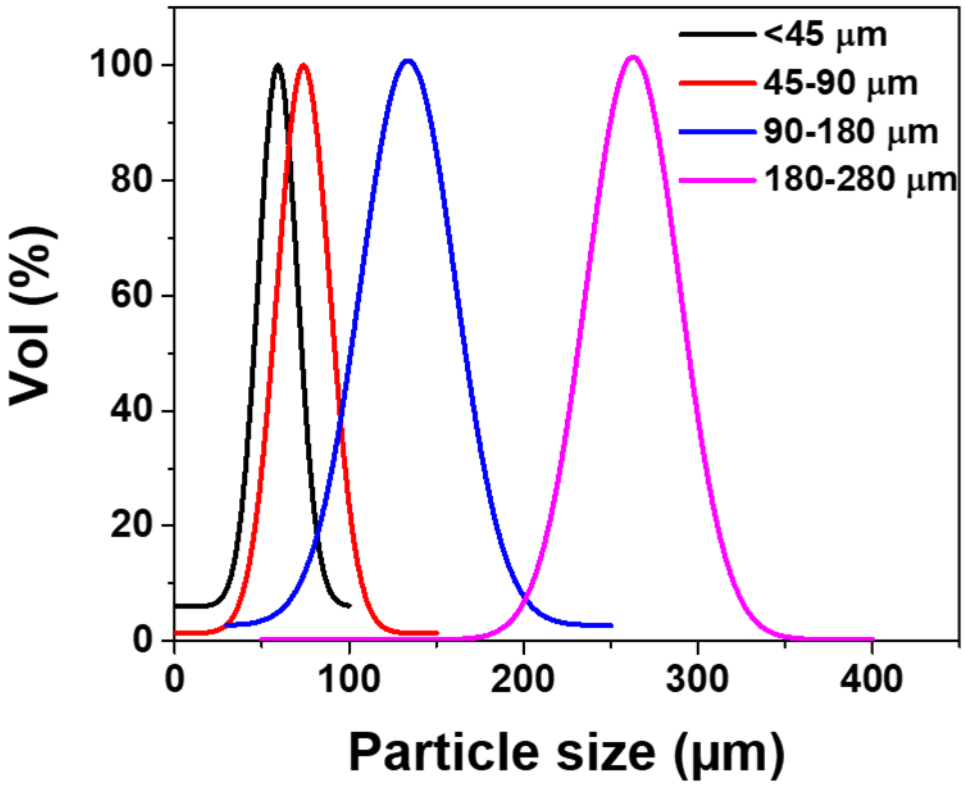

Figure 3 Particle size analysis of sieved JSC-1A samples used in sintering study. Powders were sieved three times and are shown to have over 90 count% within the selected size range.

The quality of the brick samples after sintering was apparent by visual inspection with the bricks made from the smallest particles were much smoother with very few visible holes, while the large particle bricks were visibly grainy. SEM images, shown in Figure 5(a-d), are of the compacted samples that underwent a heating profile of 1150 °C maximum temperature for a 30-minute hold. Although they experienced the same heating conditions, the samples are clearly in different stages of sintering due to the initial particle sizes. The smallest particle of JSC-1A samples (figure 5a) have shown total inter-particle bridging to the point where particle boundaries

are effectively eliminated and the sample is reaching maximum densification. The two middling samples (figure 5b,d) show a state of pore size reduction as mass is beginning to transport from the bulk material toward the inter-particle bridges to minimize the total surface energy of the sample. Larger particle samples (Figure 5d) are still forming very small inter-particle bridges and the majority of the particles are still in very well defined particle boundaries. It is also noteworthy that the less sintered samples were much easier to machine with a lathe or most saws and could be used as a material with which to make some very simple tools, screws, etc. Similar phenomenon can be seen for the MGS-1 samples in figures 5e-g, however the sintered MGS-1 samples were visibly less sintered and much more brittle compared to their JSC-1 counterparts. Samples with particles above 180 µm did not sinter enough to be removed from the mold without crumbling and samples in the range of 90-180 µm often broke while handling.

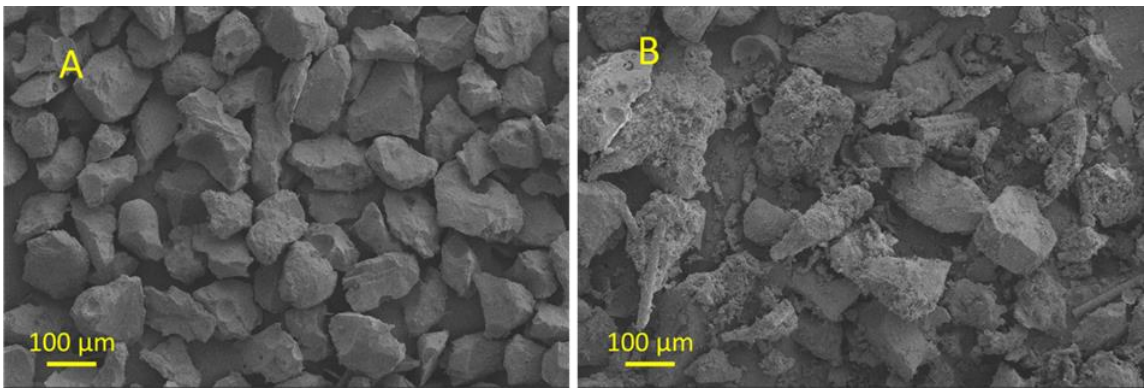

Figure 4: SEM image of A) JSC-1A and B) MGS-1, both sieved to a size range of 90-180 micron. JSC-1A is a uniform mixture of clean particles while MGS-1 has some irregularly shaped particles and particles with very rough surface topology and. This likely leads to very inneficient packing of MGS-1 in molds, even when vibrated.

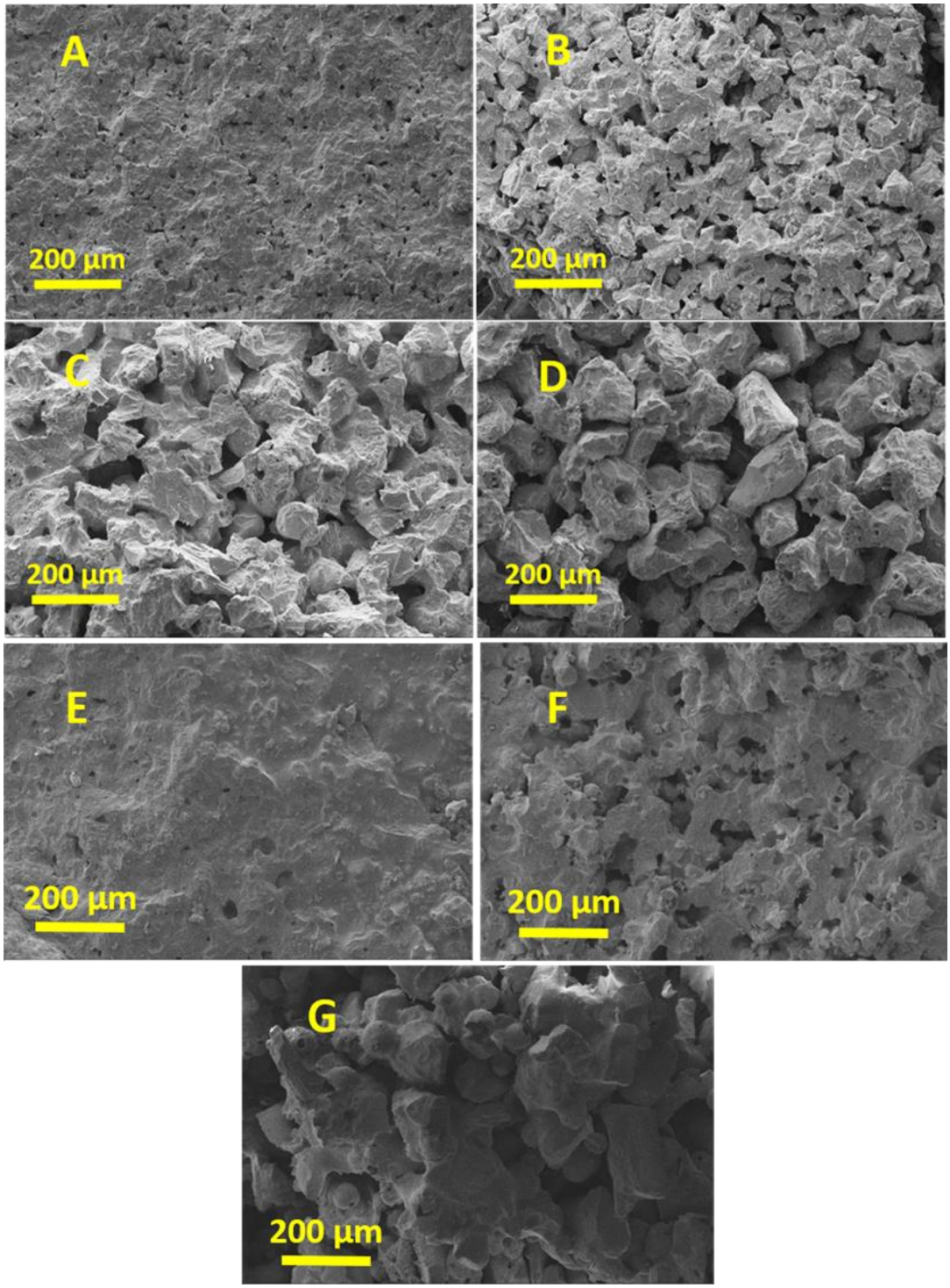

Figure 5: SEM images of sintered JSC-1A and MGS-1 bricks. Figures A-D are all of JSC-1A with particle sizes of A) <45 µm, B) 45-90 µm, C) 90-180 µm and D) 180-280 µm. Figures E-F are all

of sintered MGS-1 with particle sizes E) <45µm, F) 45-90 µm and G) 90-180 µm. All samples in these images were heated to 1150°C and held for 30 minutes. Images were taken of fragmented samples after compressive strength testing was done to expose the internal pore structure. JSC-1A samples clearly display all stages of sintering ranging from interparticle bridge initiation in image D to near complete densification in image A with pore formation and pore size reduction in images C and B respectively. MGS-1 samples also show similar stages of sintering with similar pore structure to the JSC-1A counterpart.

The movement of mobile molecules in a heated solid coordinates itself in a way so to minimize the total surface area in a solid body. Particles in physical contact with each other will have material diffuse from one particle to an adjacent particle, forming an inter-particle bridge, which eventually grows until the voids between particles are minimized or even eliminated. Sintering happens in three distinct phases with different mechanism behind each stage [55-60]. Stage I takes a loose, or "green", powders and forms loosely bound agglomerates when surface material begins forming a "bridge" or "neck" between adjacent particles. The voids between particles are still prevalent, large and generally form a network off empty space within the bulk of the solid material. Stage II begins minimizing the size of the voids until isolated pores remain between particles. This occurs as material from the bulk of a particle begin migrating toward the newly formed neck between particles to minimize the high surface area that the neck creates. After Stage II, Stage III begins to increase sample density by filling in voids until sufficiently small or even eliminated. A diagram of the sintering process highlighting different stages with examples from our experiments is shown in figure 6.

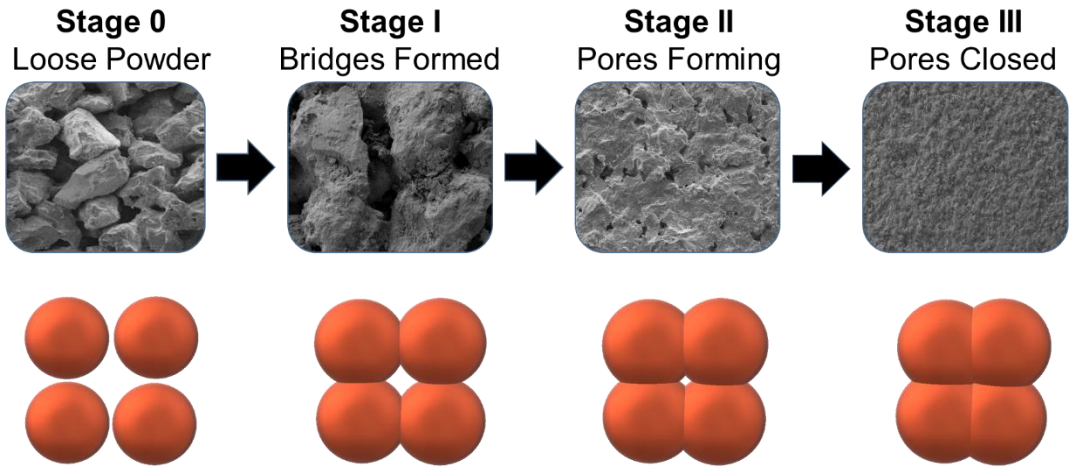

Figure 6: Sintering process for ceramic powders going from loose powder to a fully sintered, poreless solid material. This process is driven by the thermodynamic tendency to minimize total surface energy by migrating atoms between adjacent particles to form necks, and then bulk migration to close pores.

The signs of sintering equilibrium were only seen for the sample with the smallest void vol %, which was achieved by heating under 45 micron particles to 1200 ^{o}C for 30 minutes. This sample, compared to a sample of the same size range heated to only 1150 ^{o}C is shown in figure 7a,b. The internal pores in figure 7a are relatively larger than those seen in other samples (figure 7b) and are very spherical, which is not seen in any other sample. The spherical shape indicates the pores have reached equilibrium and have been given sufficient time and energy to coordinate themselves into the lowest total energy configuration as explained in the previous paragraph. This configuration of the particle interfaces and pore size and shape making the sample a low energy continuum of sintered particles is responsible for the high compressive force required to fracture this sample.

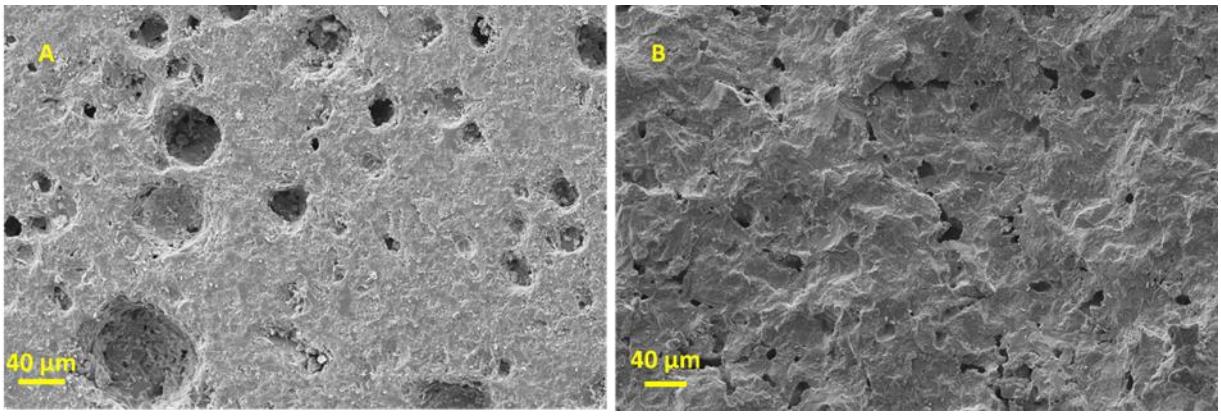

Figure 7: SEM image of under 45 micron JSC-1A powder samples. A) Sample was sintered to 1200 degrees Celsius for 30 minutes and shows pores that are around 40 micron in diameter and are approximately spherical. B) Sample was heated to 1150 degrees Celsius for 30 minutes and shows smaller pores that are uncoordinated and irregularly shaped.

To examine the physical structure of the granular material and the effect of the heat treatment on the crystallography of the simulant, x-ray diffraction (XRD) was done on samples using particles less than 45 micron that were heated to 1150°C and held for 60 minutes. The XRD patterns for the un-sintered material showed the granular material to be mostly amorphous with a series of weak diffraction peaks that would be the result of slight crystallinity from varied species of ceramics within the simulant. During the hold at 1150°C, the crystallinity of the material only changes very slightly with a disappearing of a peak around 67° from what is likely the (103) peak of the alumina in JSC-1A. During the sintering process, the alumina likely migrates to the grain boundaries, which is known to happen for alumina in high-temperature heating with an oxygen gradient within a solid [60]. Figure 8 shows the XRD patterns for the sintered and un-sintered samples. The XRD pattern for the un-sintered regolith simulant shows distinct peaks correlating to the various metal oxide material with a small signal to noise ratio indicating the material is

mostly amorphous. When compared to the un-sintered material, the sintered regolith has the same peaks present but are much weaker in intensity because much of the bulk material has moved to the grain boundaries to form inter-particle bridges, binding the powder material into a solid brick.

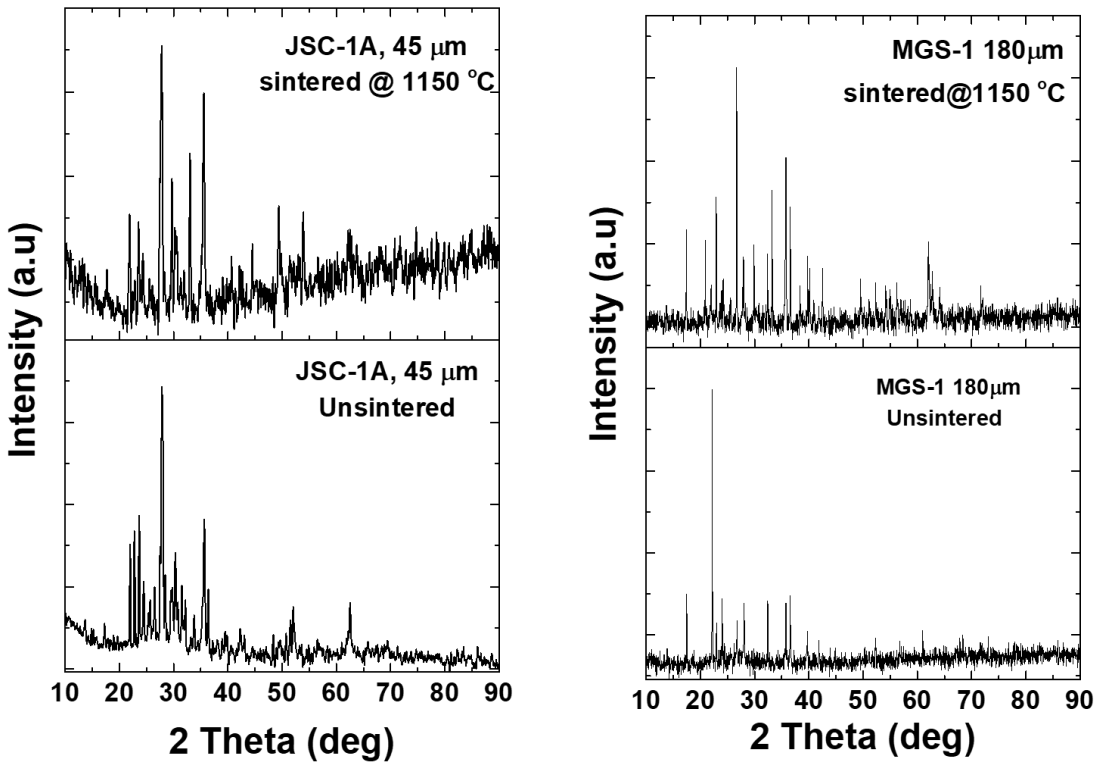

Figure 8: XRD pattern of JSC-1A (Left) and MGS-1 (right) samples with particle sizes less than 45 micron before heat treatment (top) and after sintering (bottom). The only physical change in the JSC-1A crystals is a possible elimination of the (103) peak for alumina in the material. The MGS-1 regolith undergoes significant changes in peak location and intensity.

The results of the compressive testing are shown in figure 9 and are categorized by heating profile and plotted based on the average particle size in the sample. It is quickly noted that the vibrational compaction of the loose powder prior to sintering has a large role in the strength of

the final product. Compacted powders undergoing the same heating profile as un-compacted powders showed a compressive strength nearly double that of the uncompacted bricks. This is due to the higher total contact surface area in compacted powders that allows for sintering to happen in a higher fraction of the particle surfaces. This effect is also seen in the higher porosity of uncompacted samples as discussed later. It is shown that doubling the hold time of the sintering samples from 30 minutes to 60 minutes had a varied effect on the samples depending on the initial particle size. The samples of <45 micron particles showed an 18% increase in compressive strength from the longer hold time while the 45-90 micron and 90-180 micron samples showed increases in 31% and 90%, respectively, compared to the same particle size samples that were only held for 30 minutes. This effect ties into the initial contact area of the powders as they were compacted into the molds. The larger particles had less total contact between particles and therefore the initial stages of sintering wherein bridges are formed between particles requires much more time and energy to achieve than the samples with smaller particle sizes. This delayed formation of inter-particle bridges translates to a longer time requirement for those samples to fully develop into properly sintered bricks. The samples with larger particles see a larger relative increase in strength from the longer sintering time because the larger particles take longer to transition through the stages of sintering and the longer hold time allows proper time for densification to occur in the bulk of the material while the smaller particles reach the later stages of sintering much earlier than the larger particles. The samples of <45 micron powder that were heated to 1200 °C and held for 30 minutes became a rock-like sample with no distinguishable particle boundaries and had an average yield strength of 37,280 psi, which is nearly 10,000 psi higher than what has been previously reported for low-porosity sintered samples [61]. The

samples with particles in the 45-90 micron range heated to 1200°C saw a large increase in compressive strength compared to the samples heated to 1150°C, however did not reach the same high strength as the bricks made from the smallest particles. The MGS-1 samples had a much lower compressive strength than the JSC-1A samples, reaching a maximum compressive strength of 11,170 psi which was seen in the 45-90 μm sample that underwent 1150° C heating for 30 minutes. As expected from the examination of the MGS-1 particles, the Martian simulant showed a much lower compressive strength as a result from weaker inter-particle bonding. The low strength from MGS-1 can be the result of a number of factors. First, the very irregular surface of MGS-1 particles as seen in figure 4 can result in very poor packing in the mold, even when compacted by vibration. With rough surfaces, the total contact surface between adjacent particles can be minimal which would hinder the sintering process, limiting it to few locations on the particles for atoms to migrate to in order to form bridges. This is supported by the higher porosity measurements seen in the sintered MGS-1 samples shown in table 1. The higher porosity of the sintered material can also be a result of the high volume of volatile gasses released by MGS-1 during heat treatment. This is further discussed later in this section and is supported by the thermogravimetric analysis of the two regolith powders.

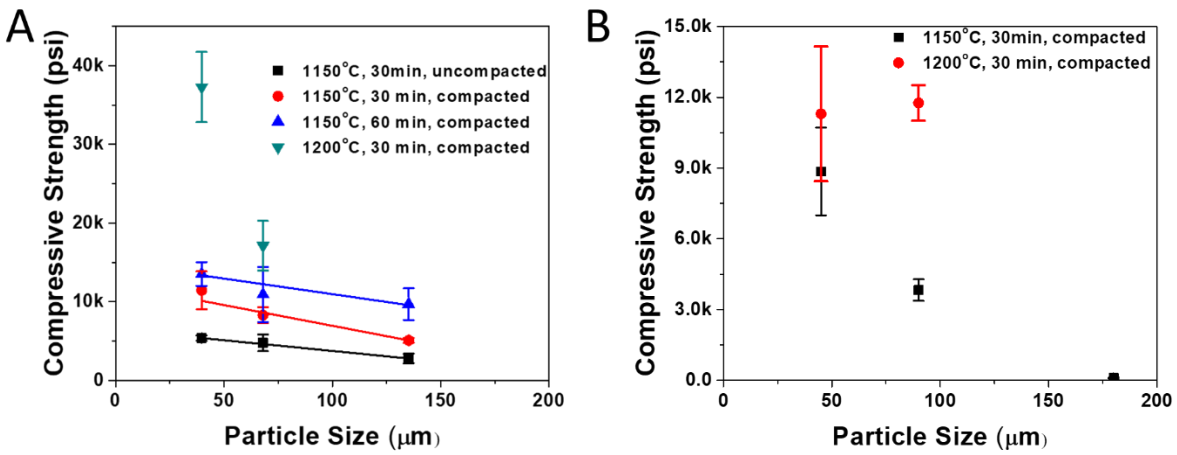

Figure 9: Compressive strength for various particle size samples and heating profile categories for (A) JSC-1A and B) MGS-1.. A trend of smaller particles samples resulting in higher is seen as well as a doubling of the final compressive strength of samples that are vibrationally compacted prior to heating. The highest compressive strength (37,280 psi) was seen by heating JSC-1A with average particle size of 38.2 micron up to a temperature of 1200 and held for 30 minutes. MGS-1 simulant did not produce the same compressive strength as JSC-1A when sintered under the same conditions, with 11,170 psi being the maximum strength achieved by MGS-1.

Table 1: Volume % porosity of sintered samples as measured by a submerssive water adsorption technique. Porosities range from over 26 vol% for the largest particle samples down to 0.22 vol% for the most densified samples. For comparison, the porosity of full melted, solidified regolith "glass" was measured at 0.16 vol%.

Heating Profile (Max temp °C, hold time minutes, compaction)	Simulant Particle Size Range (Min size, max size in µm)	Porosity (Vol %)	Error (+/-)
1150°C, 30 minutes, uncompacted	JSC-1A, (0,45)	18.21	2.66
	JSC-1A, (45,90)	18.97	1.69
	JSC-1A (90,180)	21.4	1.7
1150°C, 30 minutes, compacted	JSC-1A (0,45)	2.42	0.45
	JSC-1A, (45,90)	2.10	0.87
	JSC-1A, (90,180)	20.87	0.62
	JSC-1A, (180, 280)	26.42	2.21
	MGS-1, (0,45)	0.51	0.12
	MGS-1, (45, 90)	13.85	0.85
	MGS-1, (90, 180)	43.5	2.98
1150°C, 60 minutes, compacted	JSC-1A, (0, 45)	0.40	0.16
	JSC-1A, (45,90)	1.51	0.45
	JSC-1A, (90,180)	6.53	2.0
1200°C, 30 minutes, compacted	JSC-1A, (0,45)	0.22	0.1
	MGS-1, (0,45)	0.80	0.15
	MGS-1, (45-90)	0.94	0.12
Melted and cooled to a glass	JSC-1A, N/A	0.16	0.05

The porosity measured from the fragmented samples showed a large correlation between initial particle size, heating profile and final porosity. As expected, the smaller particle samples produced much more dense products and the higher and longer heating profiles had a similar effect. The porosity is summarized in Table 1. An interesting relation is seen when plotting the compressive strength of samples against the final porosity regardless of the heating conditions (figure 10). There is a negative power law relation between porosity and strength when samples with nearly zero internal pores are included, which has not been seen previously in literature. Indyk, et al published a data on sintered JSC-1A simulant, which compared the strengths and porosities of two samples and concluded the relation between the two properties was linear leading to a theoretical maximum compressive strength lower than is achieved in this study [61].

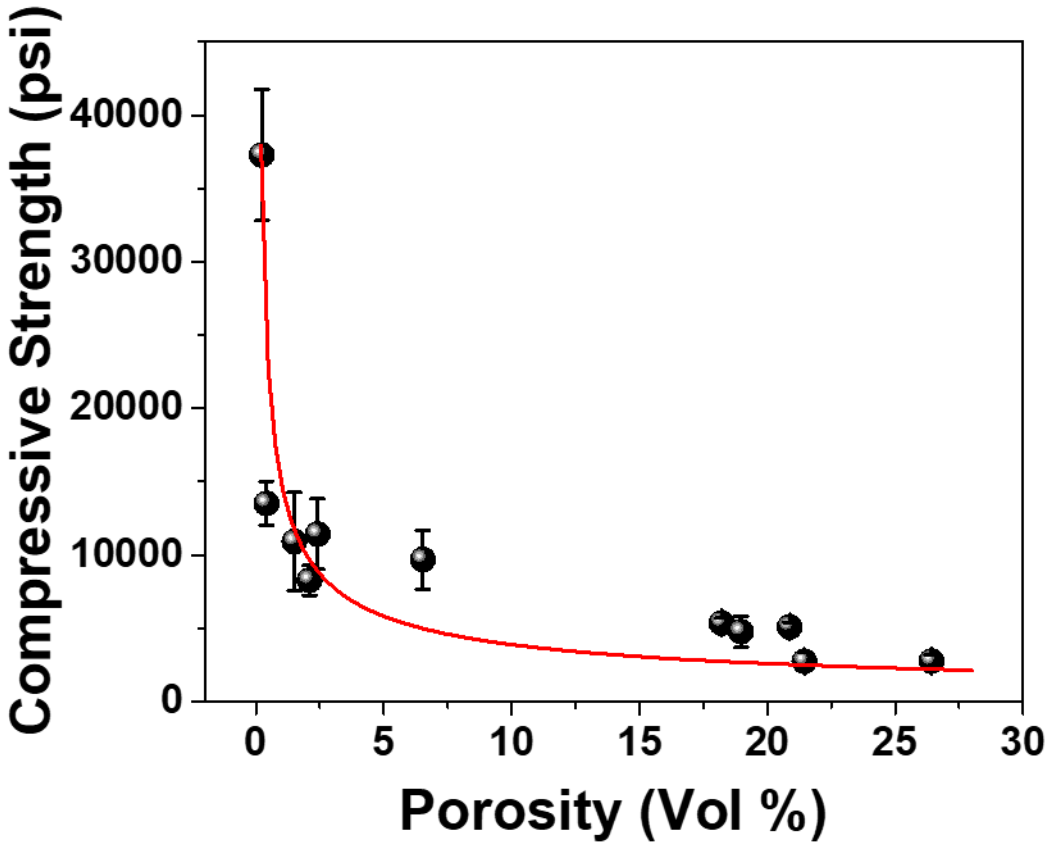

Figure 10: Compressive strength of samples vs porosity of samples. A clear negative power law relation is seen in sintered samples as the sample with 0.22 vol% pores shows an enormous increase in compressive strength from the samples that averaged between 1 or 2 vol% pore. Samples between 1 and 30 vol% pore show a compressive strength in agreement with current literature.

Despite compaction prior to sintering, there exists a maximum packing factor of the powder, which allows for pockets of air within the green powder compact. These air pockets will form internal pores in the bulk material and ultimately prevent complete densification unless the

powder material is melted and re-solidified. For two particles in contact with each other during the sintering process, the contact angle will increase from zero until it reaches a critical angle, called the dihedral angle, at which the surface energy of the particles equals the interface energy between the particle grains and an equilibrium is reached [56]. For the voids adjacent to sintering particles, equilibrium is reached when the energy of the total particle-void surface balances with the energy of the particle-particle surface. For this reason, the pore size and shape is heavily dependent on the number of surrounding particles, which is called the coordination number. The coordination number combined with the dihedral angle give criterion for the pore stability, size and shape [54,55]. The minimization of surface energy is the force driving the pore to decrease in size this force is pointed radially inward for the spherical pore and is countered by the force minimizing the interfacial energy. At full equilibrium of the pore structure, the curvature of the shape is minimized into spheres due to the vacancy migration from high curvature areas and relies entirely on surface transport mechanisms rather than bulk transport mechanisms, meaning no change in density occurs during that process. The reduction of size of the pores that develop within a sintered material is controlled by grain coarsening and requires that the coordination number for the pore be sufficiently small to allow the total change in energy to be negative.

To understand another possible cause of the difference between JSC-1A sintering and MGS-1 sintering as well as porosity of the final product, thermogravimetric analysis was done on 45 μm powder from each sample. They were heated up to 1500°C at a rate of 20°/min in inert gas. Figure 11 shows the weight loss of each sample during this process, and MGS-1 loses over 15% of its weight by the time it approaches 1200°C, with the most dramatic weight loss happening right at the temperature we sintered the material for this study. In this same temperature

range, JSC-1A has only lost 5 % of its weight. Volatiles and bound water that get released during heating of regolith is a topic of research as a means of collecting water on the moon or Mars, but for this application hydrated minerals in the regolith may hinder the sintering process, causes brittle, porous bricks to form as gasses are being released at the same temperatures. The loss of volatiles such as water from the grain of the regolith can cause the drastic change in XRD pattern seen in figure 8. The MGS-1 simulant is composed of hydrated minerals – appropriately so- to mimic the reality of Martian regolith. The mineralogical changes to the regolith that occur during the heating process happen while the powder undergoes sintering, making it difficult to distinguish one potential cause of the change in XRD pattern from the other. Chemically, the two simulants are very similar in that they both contain primarily iron oxide, silica, alumina and other oxidized metals, making it unlikely that the change in XRD pattern seen when sintering MGS-1 is from a phase change of the chemical components since JSC-1A contains the same chemicals and does not see a similar peak change in XRD.

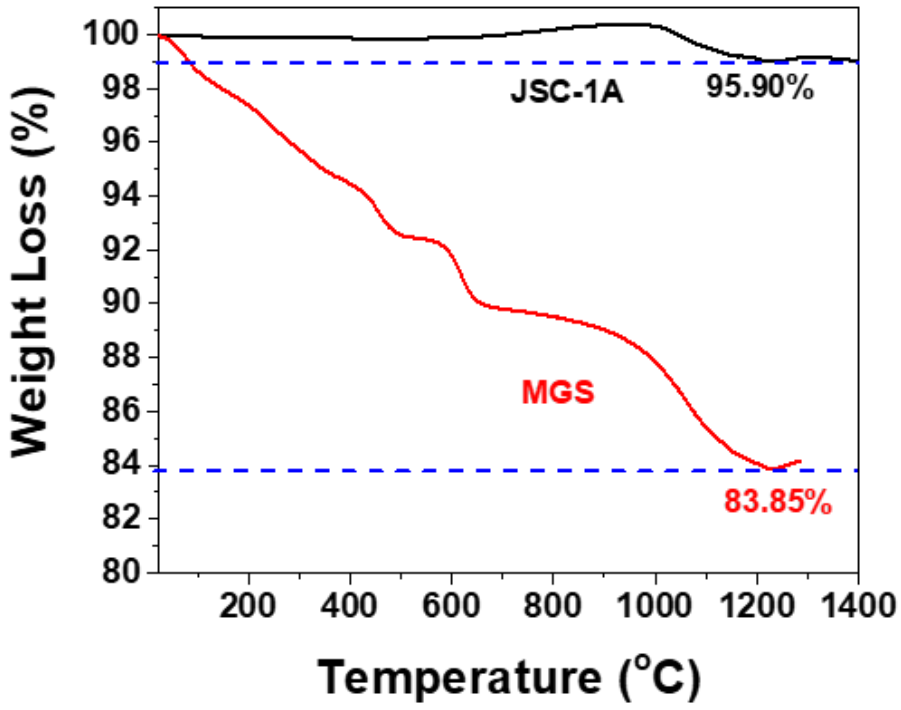

Figure 11:Thermogravimetric Analysis of JSC-1A and MGS-1 powders less than 45 µm. Samples were heated beyond 1200 degrees Celsius and showed very distinct weight loss curves. JSC-1A lost less than 5% of its original weight to volitalization of components engrained in the particles crystal structure. MGS-1 lost well over 15% of its weight from volatilization, with the most dramatic weight loss happening in the temperature range in which sintering takes place.

The technique of sieving powder and then pressing and heating could be feasible to employ in a lunar environment. The regolith taken from multiple sites of the Apollo 12 and 14 missions, as well as other missions, had a median grain size of 0.05 mm to 0.735 mm and went as low as 40 mm [62,63]. This means the powders could be sieved to the sized used in this experiment without any extra processing. The results from sintering on the lunar surface should be close to

the same if real lunar regolith was used because JSC-1 A is very similar as mentioned earlier. However, it should be noted that some areas do have different compositions and there could be variation depending on where the soil is harvested from on the lunar surface [64].

2.2 Nano-Functionalization of Regolith for Cementation

Alternative methods of binding regolith particles have been studied as excitement for future missions to colonize Mars or the moon has grown. Most methods of binding regolith together involve addition of a thermoplastic such as polyethylene, which has the advantages of being found as packaging material and other objects that would otherwise be considered disposable. These methods of binding regolith into a solid material rely on trash material which is limited in quantity for any given mission. It is possible to manufacture plastics on Mars by extracting CO_2 from the atmosphere and converting the gas into the monomer ethylene as discussed in Chapter 1. The production of ethylene from a Sabatier reaction is still an area of active research and the development of a compact reactor with efficient catalysts is still some time away. Other methods of compacting regolith involve using ice as a binder for powder regolith, which requires structures exist in a region of Mars of the moon that's permanently frozen which is almost nowhere in the case of the moon, and exclusively the poles of Mars. A method for compacting regolith from sustainably sourced materials without the enormous energy requirements of sintering is still needed for colonization efforts. The method studied for this chapter binds regolith particles together via a nano-functionalization technique that can be used for any alumina-silicate material.

This low temperature cementation process can be utilized for any alumina-silicate powder including fly ash, beach sand or regolith, making it a technology useful for both space and

terrestrial application and was initially developed by Dr. Sudipta Seal, Dr. David Reid and Dr. Larry Hench to produce a zero CO_2 emission concrete alternative from waste products such as fly ash and sand [65] . The cementation is split into two reactions. First, the powder is mix with sodium hydroxide to react with the surface silicon and aluminum, depositing sodium atoms onto the surface of each particle according to the following reactions:

$$SiO + 4NaOH \rightarrow Na_4SiO_4$$

Or

$$Al_2O_3(s) + 6NaOH(aq) + 3H_2O(l) \longrightarrow 2Na_3[Al(OH)_6](aq)$$

The modified surface of the powders are then reacted with ethanol to functionalize the modified surface with hydroxyl terminated alcohol chains, which combine to form oxygen bonds between particles. The slurry of particles is then poured into a mold and heated to cure into solidified bricks. The curing process lasts up to 28 days and the entire reaction requires heating only up to 120°C. The synthesis process is summarized in figure 12. Previous studies of this technique using sand or fly ash as an agglomerate have been studied as a method of producing environmentally friendly cement with zero carbon emission. Compressive strengths of the cemented sand exceeded those of traditional Portland cement.

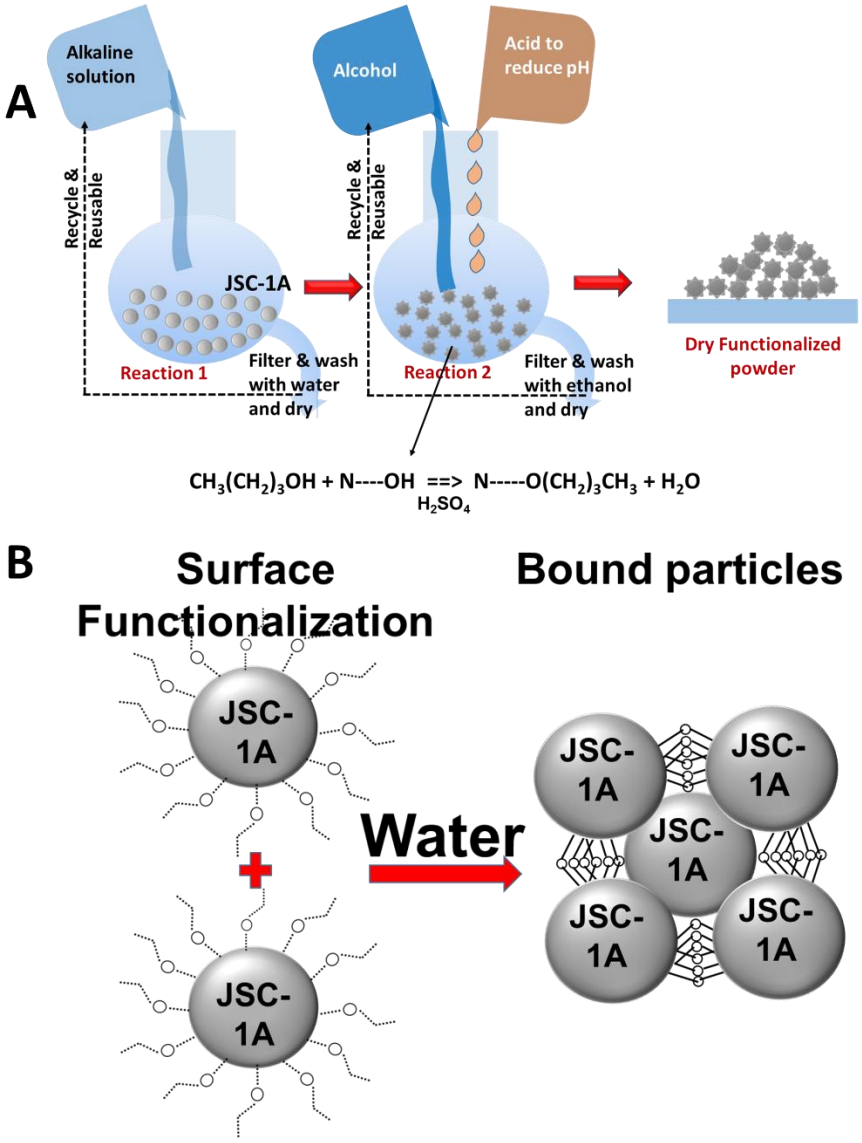

Figure 12: Cementation process for nano-functionalized alumina-silicate particles.(A) Alkaline solution reacts with alumina or silica species to form OH species on the surface of particles, which will (B) form oxygen bonds between particles in the presence of water. These oxygen bonds allows powder to form into a solid brick. JSC-1A was used as an aggregate to form a brick from this process.

This process was implemented on lunar regolith simulant JSC-1A to make bricks for compressive strength testing. Two sets of three bricks were synthesized and cured in cylindrical molds with a height-to-width ratio of 2:1. One set was cured for 21 days and the other for 28 days and then tested using a Syntron compressive strength tester. Figure 13 shows the results of the compressive testing and the synthesized samples had a compressive strength of the 21-day and 28 day samples were 3000 and 3300 psi respectively. This is roughly the same strength of Portland cement and that seen in similar samples made from sand and fly ash [66,67].

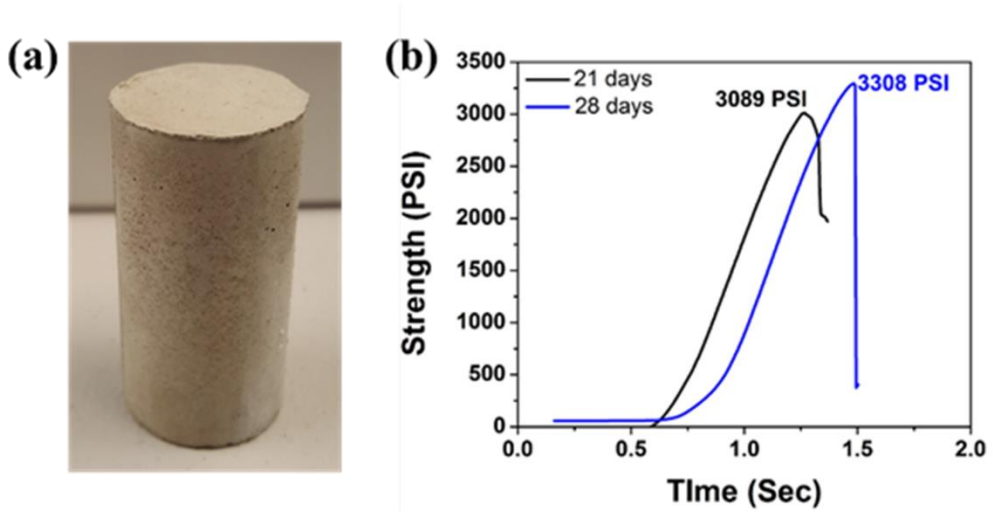

Figure 13: (A) Compressive strength test coupon produced from JSC-1A powder using nano-functionalization technique described above. (B) Compressive strength results from two sets of samples with different curing times. Each set of samples is comparable in compressive strength to Portland cement with compressive strengths of 3089 and 3308 psi. Typical Portland cement is around 3000 psi depending on the aggregate used and processing technique.

While the compressive strength of the nano-functionalized brick samples were not a high as the sintered samples, this process does provide certain advantages over the sintered material

which could be implemented for certain applications on a lunar or Martian colony depending on the overall architecture of the colony. The low reaction temperature of the process offers a low-energy requirement for production of cement-like material compared to the sintered regolith material. This material may be advantageous for use in structures without much structural load requirement like walkways, dust barriers, and radiation barriers due to the lower compressive strength of the material compared to the sintered material. The nano-functionalized material also bears material requirements beyond the aggregate regolith powder. Sodium hydroxide (or alkaline salt), alcohol and water are required to produce these bricks. Recent discoveries of salty water at the poles of the moon suggest a possibility of the appropriate salts being present to utilize this technique [68]. Water is prevalent on Mars and somewhat on the moon, however, it may not be optimal to use for construction material, despite being possible to recycle at least 90% of the water used in this process. Alcohol can be found as a volatile bound within the grains of regolith powder found on the surface layer of mars and the moon. Current architecture plans for ISRU involve processing plants to collect volatiles such as alcohol in the regolith by heating batches of regolith and pumping out resulting gasses to be further processed. The limiting material in the process from an ISRU perspective is the sodium hydroxide used in the initial phase of the reaction. While sodium and hydroxides have both been separately detected on the surface of Mars [69], it is unclear if hydroxide minerals exist on the surface of the moon.

CHAPTER THREE: FERROSILICON AS A FEEDSTOCK FOR ADDITIVE MANUFACTURING PROCESSES

Ferrosilicon was studied as a candidate feedstock material for wire-based 3D printers designed for in-space manufacturing. Given that the prototype MRE reactors have failed to withstand the high temperatures and corrosiveness of the regolith melt [37], simulated versions of the products of that process are used for this study as a way to prove the utility of the MRE process while the reactor is being developed. While real-world products of the MRE process will be "mongrel metals" with impurities and non-uniform composition, processes to refine these metals are a subject of future work and a pure, well produced alloy of iron and silicon will serve as an adequate simulant for these materials as a starting point for investigations. Ingots of composition ranging from pure iron to 12 wt% Si were synthesized and made into rods for mechanical testing to determine ultimate strength and ductility. It was determined that the samples above 3 wt% Si were too brittle to be pulled into wire and ruptured with very little strain. The 3 wt% Si sample and iron had comparable mechanical properties relative to higher silicon content samples but with differences in ductility and ultimate strength. Microstructure and compositional studies revealed the differences between the ductile and brittle samples as being the complete ferrite phase presence on the iron and low-Si content samples. This study puts an upper limit on the useable materials derived from Martian and lunar regolith as 6 wt% Si.

3.1 Broad Ferrosilicon Characterization

With little known about the mechanical and electrical properties of ferrosilicon, characterization of a broad range of compositions was done to determine the portion of the phase diagram most relevant to our application of 3D printing. To produce ferrosilicon, samples of steel grade iron powder and 25 wt% Si in Fe powder were obtained from GKN and analyzed for chemical accuracy. The powders were mixed together in proportions based on a target silicon content. The mixed powders were then placed in an alumina crucible coated with a zirconia paint to allow removal of solidified samples from the crucible. The crucible was then placed in a Deltech bottom-loading furnace and ramped up to at least 1600°C in 2 hours, held at that maximum temperature for 30 minutes, and allowed to cool naturally in the closed furnace.

The first iteration of ferrosilicon samples included four target compositions to get a broad understanding of the range of characteristics; 75. wt% Si, 34.0 wt% Si, 20.5 wt% Si and 6.0 wt% Si. The high form crucibles proved to be adequate to make thick samples and minimize the

oxidation of the samples, one of which is shown in figure 14.

Figure 14: 6 wt.% Si in Fe ingot produced from GKN powders in Deltech furnace.

Figure 15 shows an example summary of elemental characterization done on the FeSi samples to ensure the composition of the produced metals matches the targeted composition. The composition of each sample was measured using a Zeiss ULTRA FEG SEM. This was done to accurately correlate the true composition of the sample with the measured mechanical and electrical properties. The elemental analysis of the remaining samples is summarized in table 2.

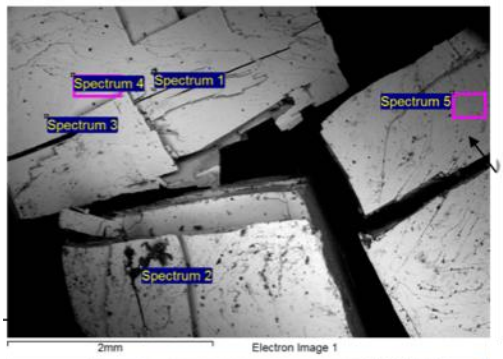

Spectrum	In stats.	O	Si	Fe	Total
Spectrum 1	Yes	1.13	5.48	93.39	100.00
Spectrum 2	Yes	61.43	14.33	24.23	100.00
Spectrum 3	Yes	0.85	5.56	93.59	100.00
Spectrum 4	Yes	1.46	5.59	92.95	100.00
Spectrum 5	Yes	2.70	5.24	92.06	100.00

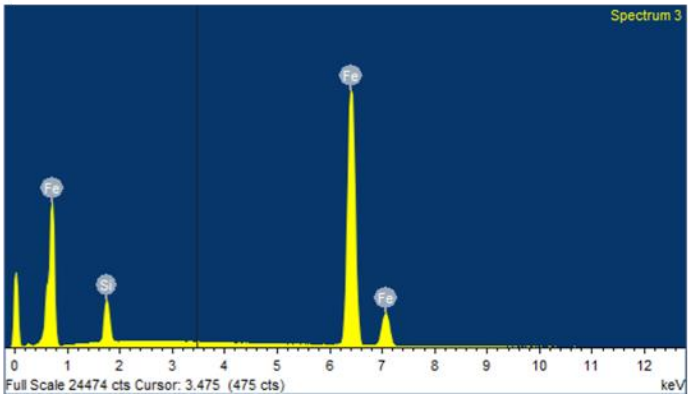

Figure 15 EDXS/SEM analysis of FeSi6. Left: images of FeSi6 pieces. Right: Measured values from EDXS spectra of selected areas (specific on left picture) and results of spectral analysis on composition.

Table 2: Summary of compositional analysis from first iteration of FeSi samples.

Target Composition	Si Content (Wt%)	Fe Content (wt%)	Other (wt%)
6 wt% Si	6.7 +/- 0.6	92.7 +/- 0.4	0.5
20.5 wt% Si	23.5 +/- 4.4	74.8 +/- 2.4	1.7
34 wt% Si	37.5 +/- 8.8	62.0 +/- 8.2	0.5
75 wt% Si	71.6 +/- 2.9	26.7 +/- 2.4	1.6

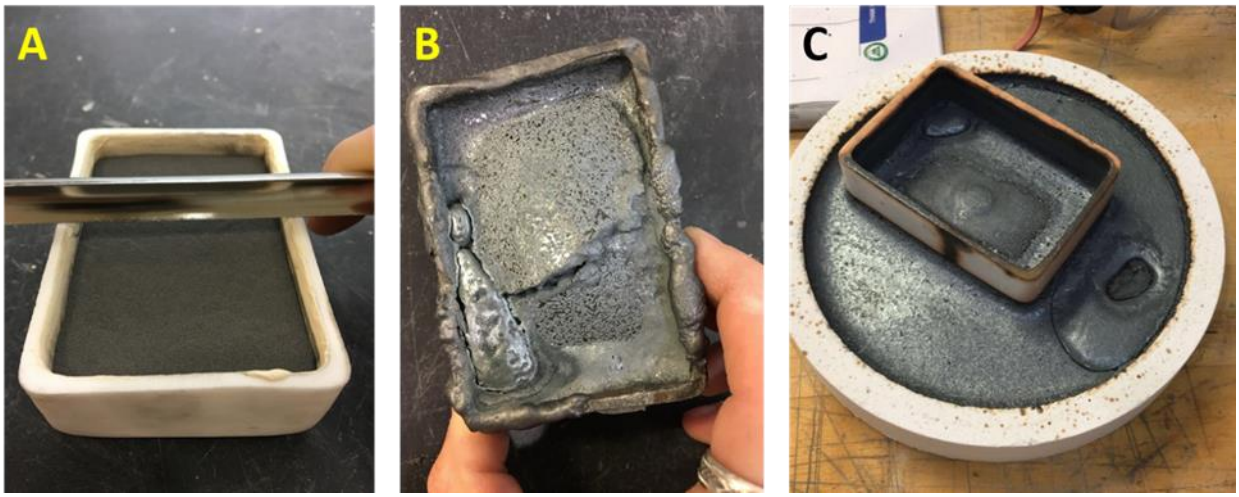

Figure 16: Alumina crucibles filled with a mixture of pure iron and 75 wt.% FeSi before melting (A, representative) and after their respective melting (B, C). Due to the open atmosphere design of the furnace, the iron powder oxidized during the heating and began reacting with the alumina in the crucible, often times eating through the walls of the crucibles.

Synthesizing alloys in the flat geometry of ASTM tensile strength coupon standards was met with failure in the air furnace. The combination of the use of iron and ferrosilicon powders and the high surface-to-thickness ratio of the crucibles resulted in rapid oxidation and high kinetics reactions between the formed iron oxides and the alumina crucibles; this resulted in the loss of material (figure 16). The successful samples were characterized for their hardness and electrical properties to identify a favorable part of the FeSi composition spectrum for following iterations. Hardness was measured using a Vicker's hardness tester and electrical resistivity was measured using a Signatone 8" four-point probe.

In coordination with private companies developing relevant technology, an ideal feedstock for a wire-based 3D printer would have high electrical conductivity and high ductility. The

deposition of material from the wire requires running a high current density through the bulk of the material and ductility is required to ensure a spool of feedstock material will not break during production or utilization. From the characterization of the first iteration of samples, a relationship is seen between the silicon content and the mechanical and electrical properties that show the lower silicon section of the phase diagram will have optimal properties for our intended application.

The optimal wires for metal additive manufacturing will be those with high electrical conductivity and from the resistivity measurements of the FeSi samples, that characteristic emerges on the low-Si end of the compositional spectrum. This is to be expected, as Fe is a strong conductor of electricity while Si is considered a semi-conductor. Figure 17 shows the resistivity measurements of the synthesized FeSi samples spanning the composition range from 6 wt% Si to 75 wt% Si. The lowest resistivities, which makes for an optimal electrical wire are seen on the low end of the composition spectrum, as expected considering the electrical properties of silicon. Optimal mechanical properties seen on the low end of the compositional spectrum. The hardness data (figure 18) also shows a substantial decrease in the sample with 6 wt% Si compared to the other samples. The hardness and resistivity data is summarized in Table 3 below.

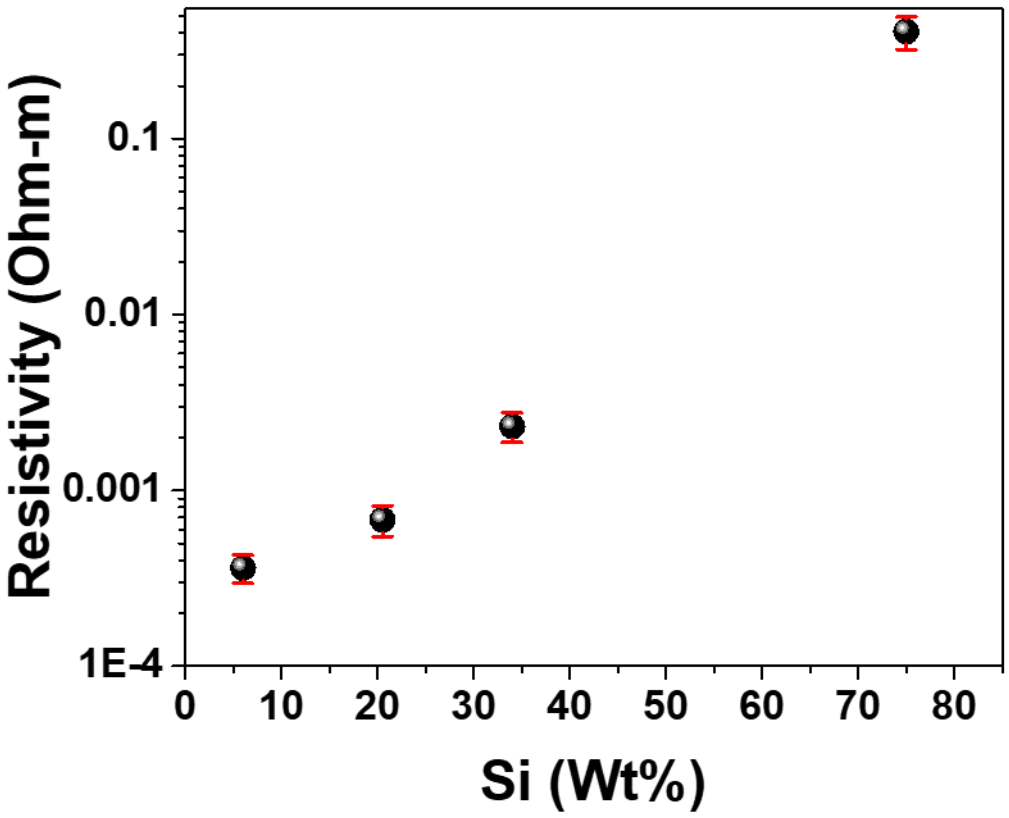

Figure 17: Resistivity measurements of the produced FeSi samples (Note: Y-axis is on log10 scale.) Samples with lower silicon content have the lowest resistivity and therefore the highest electrical conductivity

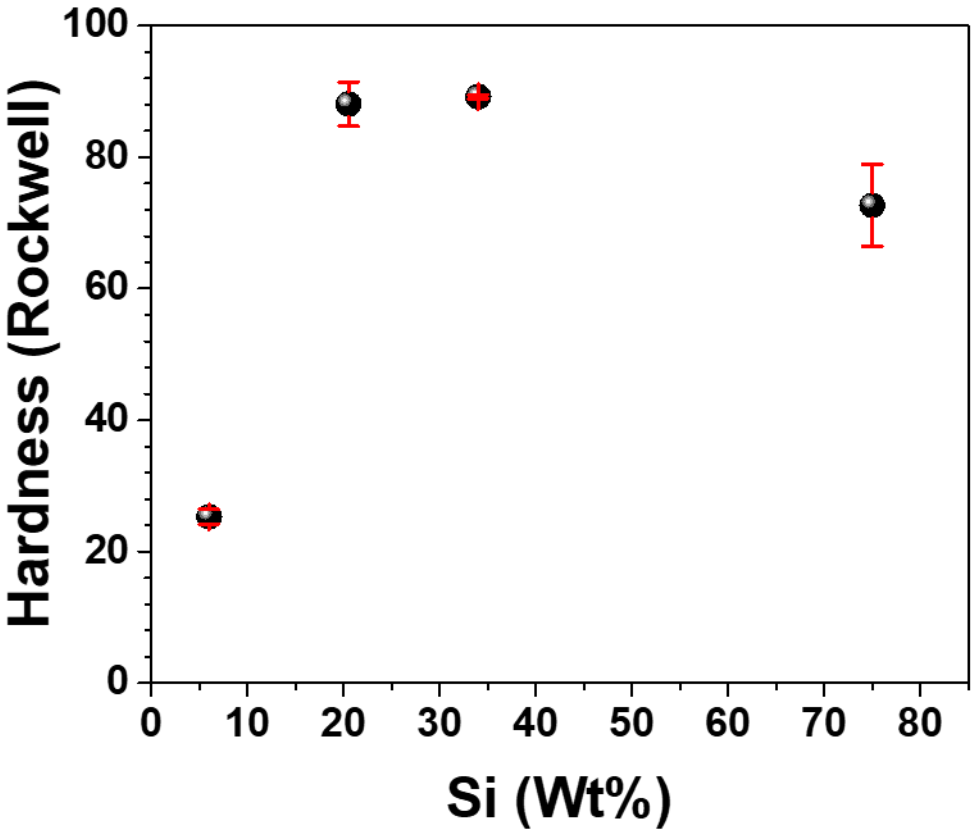

Figure 18: Hardness measurements of produced FeSi samples using the Rockwell scale. An increase in silicon content lead to increasing hardness up to a maximum value and increased brittleness.

Table 3: Summary of mechanical and electrical data collected on samples

Sample	Hardness (Rockwell)	Error Hardness (+/-)	Resistivity (ohm-m)	Error resistivity (+/-)
FeSi 6	25.3	1.1	3.62E-4	6.5E-5
FeSi 20.5	88.1	3.3	6.80E-4	1.35E-4
FeSi 34	89.2	0.3	2.31E-3	4.4E-4
FeSi 75	72.2	6.2	1.57E-2	2.26E-3

Lower hardness is desirable for drawing a wire due to the implied ductile nature of softer metals. The higher Si-content ferrosilicon alloys were also noticeably more brittle than the lower Si-content metals, which looked and behaved more like stainless steel. Ductility higher than that of common steel is required to reduce the diameter of a wire to 0.76 mm (0.03") by drawing techniques. The hardness data collected in this project indicated that this could be achieved within the ferrosilicon system by targeting the low-Si end of the phase diagram to obtain both ductile materials with low electrical resistivity to use as feedstock wires in the developing 3D metal printing technology. Efforts were thus focused to making FeSi feedstock within the low silicon content end of the composition spectrum in the second iteration of FeSi characterization.

3.2 Low Silicon FeSi Characterization.

The analysis of the first iteration of ferrosilicon samples guided the synthesis of the second generation of samples. For the second iteration, samples were made in the low-silicon range of ferrosilicon, and were compared to a sample of pure iron as a control. Target compositions were chosen to be 3, 6, 9 and 12 wt% Si. In the steel-making industry, 2 or 3 wt% Si is considered to be high and increases in the silicon content will eventually cause the metal to become brittle. The

purpose of this study is to identify a maximum on the composition of ferrosilicon that would be useful for 3D printing and other colonization applications to guide future developments of the MRE reactor. Post-processing of the products of the MRE reactor will require a step to refine the metal slag to a certain purity of metals that is considered workable. The goal of this iteration of the study was to determine the resistivity in this range of the composition spectrum as well as the mechanical properties of the bulk metal to determine feasibility as a construction material.

In order to eliminate the oxidation of samples during processing, we synthesized the second iteration of FeSi alloy ingots under controlled atmosphere at UCF's Advanced Materials Processing and Analysis Center in an ABJ-900 Arc Melter. Melting the samples under an inert atmosphere, as opposed to using the open-air furnace at Kennedy Space Center, provided higher quality ingots with more precise compositions due to the minimization of the metal atoms reacting with oxygen. A new set of 60 g samples were synthesized with target compositions of 3, 6, 9 and 12 wt.% Si using pellets of pure iron and pure silicon purchased from Alfa Aesar. Figure 19 shows an example ingot from the arc melter.

Figure 19: FeSi6 (6 wt% Si) ingot produced from arc melting.

In order to ensure an even distribution of Si within the metal ingots, the iron and silicon metal chunks were melted into a solid piece which then rapidly cooled, was flipped over, and re-melted with an electric arc. This process was repeated four times to ensure homogeneity. The arc melter enables the synthesis of ingots without oxidation but is not suitable for the molding of samples into shapes such as rods or flat bars and sheets. Several attempts to cut ingots into ASTM standard coupons for tensile strength testing were unsuccessful with the tools at both the GMRO and the Materials Science Branch at Kennedy Space Center. To determine mechanical properties of the material relevant to wire-drawing and structural manufacturing, each ingot was cut into shapes thin strips by an electric discharge machine (EDM) and placed into ceramic tubes (Coorstek item # 66301, 0.188" ID), capped with fiberglass to minimize air flow and re-melted in the Deltech furnace. The tall, thin aspect ratio of the tubes as well as the ceramic cap placed onto the opening of the tube act to minimize air circulation in the volume wherein the metal samples rest, thus minimizing any oxidation that might otherwise occur. The samples were ramped up to 1575° C in 45 minutes after which the furnace was shut off and the samples were allowed to cool naturally overnight. The cooling procedure was chosen over a quenching procedure after initial attempts at quenching from temperatures between 600°C and 650°C resulted in brittle samples. Three bend test samples of each composition including pure iron were synthesized and tested. The produced ferrosilicon rods were used as bend testing coupons to determine flexural strength and flexural modulus of the material. These two characteristics serve as an indicator of the ductility of the material as well as the tensile strength of the material.

The composition of the ferrosilicon ingots (table 4) for each sample is reached within the margin for error and the chemical analysis showed an oxygen content less than 2.0 wt% with the

Fe(12 wt%Si) alloy sample being the largest with 1.9 wt%. The higher Si content samples were more prone to corrosion and tarnishing, which is prevalent in the microstructure analysis. Figure 20 shows the metallurgical images from the polished and etched samples. The pure iron and Fe 3 wt% Si samples showed very similar ferrite microstructures, however the Fe (3 wt% Si) alloy had smaller grains than the pure iron sample. The 6 wt% Si sample showed a very irregular structure from the other samples, and displayed islands of pearlite-like structure in a matrix of ferrite. Ustinovshchikov et al [70], described the region of the phase diagram in which a B2 phase exists and will form a solid solution with the pure α phase of iron. Ustinovshchikov examined the microstructure with TEM and described this phase as {100} layers consisting entirely of silicon sandwiched between {100} layers of iron. Figure 21 shows an optical image of the B2 phase of alternating layers of silicon and iron seen in the sample with 6 wt% Si. The article goes on to describe the region above 15.5 at % (roughly 5.2 wt%) as being too brittle to form foil for TEM sample production. The authors also noted that samples below 8 at% (roughly 2.69 wt%) remained single phase. The Fe (9wt% Si) and Fe(12 wt% Si) alloy samples likely cooled slow enough to eliminate the formation of α2 and instead formed entirely α-ferrite phase. These samples showed corrosive pitting from the etchant and revealed no distinctive microstructure.

Table 4: Compositional analysis of ferrosilicon samples measured from EDX.

Target Composition	Measured Composition		
	Fe	Si	O
Fe(3 wt% Si)	96.15 +/- 0.81	2.84 +/- 0.85	1.02 +/- 0.37
Fe(6 wt% Si)	93.13 +/- 0.21	6.15 +/- 0.08	0.72 +/- 0.13
Fe(9 wt% Si)	89.29 +/- 1.87	9.22 +/- 1.68	1.49 +/- 0.77
Fe(12 wt% Si)	85.72 +/- 1.19	12.36 +/- 0.40	1.92 +/- 0.78

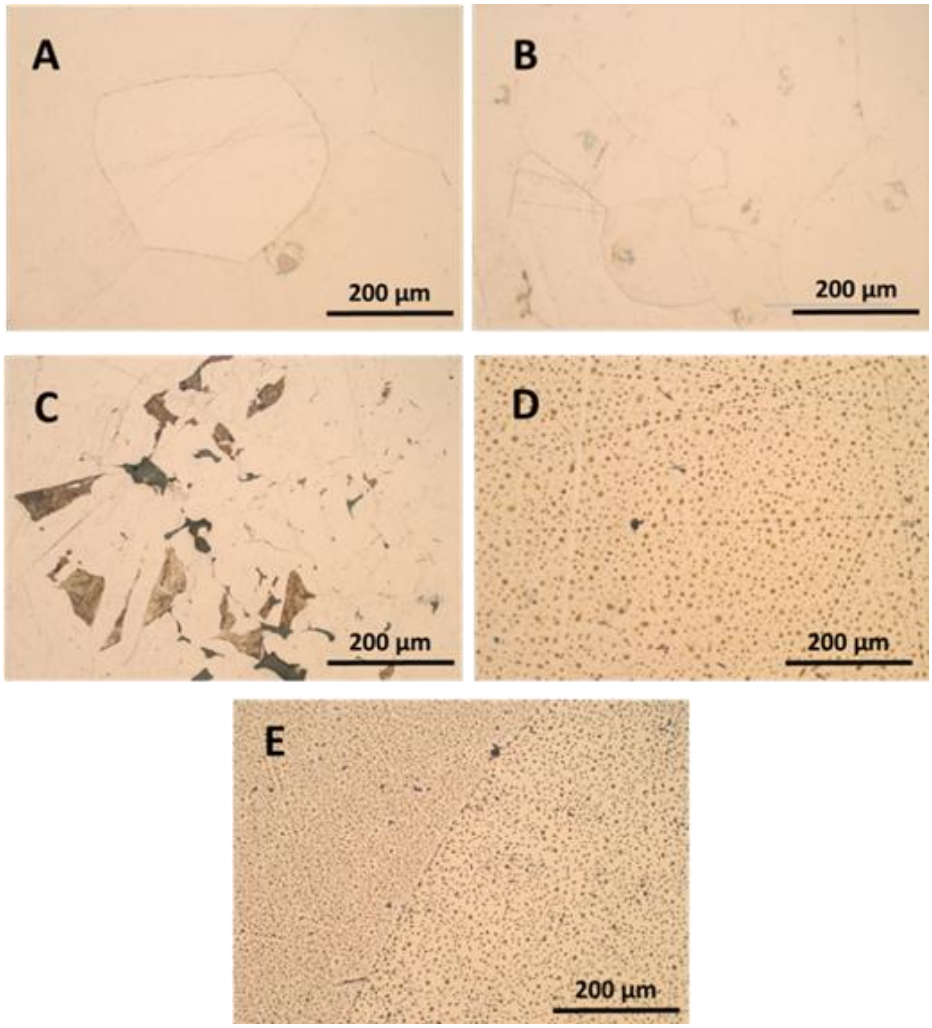

Figure 20: metallographic microscope images of polished and etched ferrosilicon samples; (a) pure iron, (b) Fe(3 wt% Si), (c) Fe(6 wt% Si), (d) Fe(9 wt% Si) and (e) Fe(12 wt% Si). The pure iron sample as well as Fe(3 wt% Si) alloy show ferrite structure as a result of cooling from austenite. The Fe(6 wt% Si) alloy has a segregated mixture of ferrite with pearlite-like islands in the metal. The α2 phase of the FeSi phase diagram exits at room temperature around 6 wt% Si and this sample cooled slowly enough to allow for nucleation of this phase. The 9 and 12 wt% Si samples did not show any distinguishable features from the etching process, but rather corroded with pitting seen on image d and e.

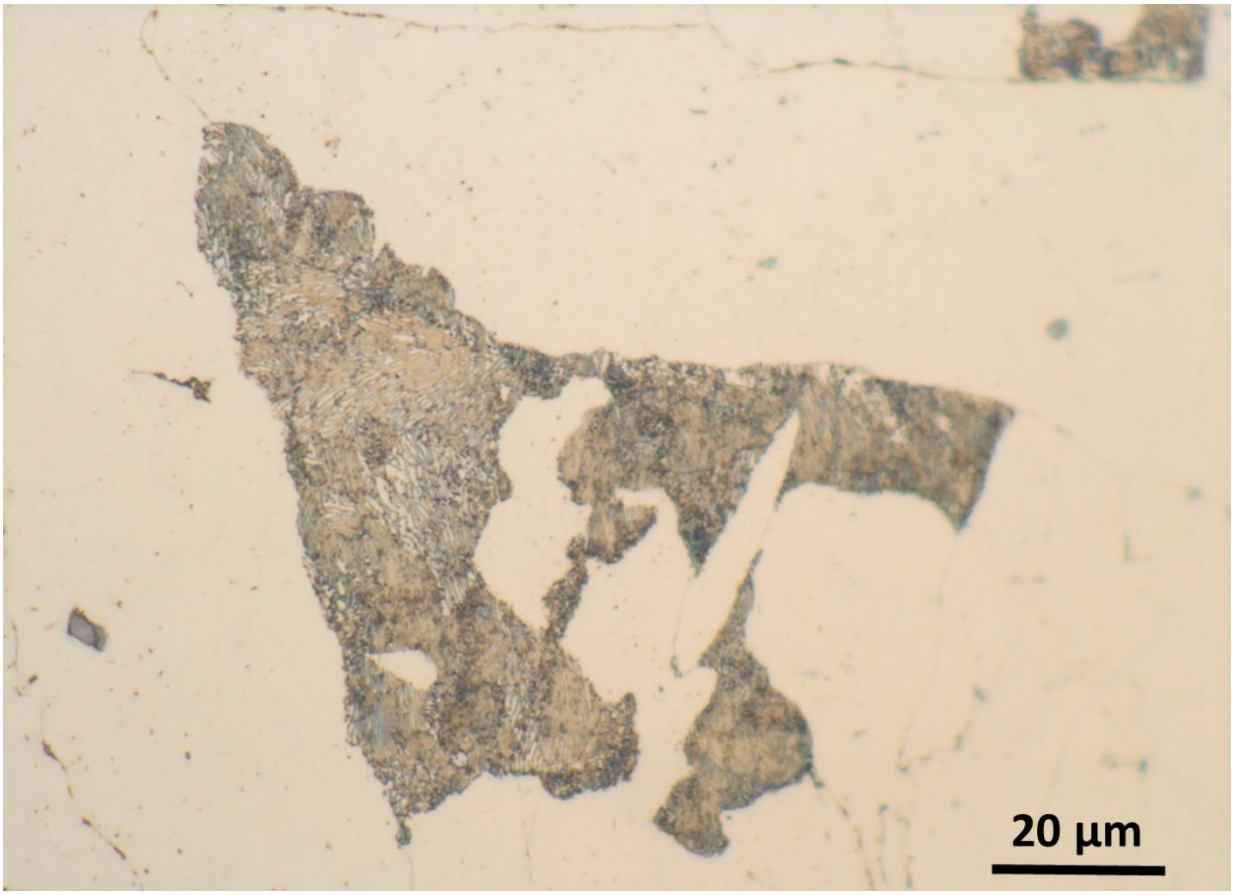

Figure 21: Optical image of Fe(6 wt% Si) sample. A grain of B2 phase is seen in the ferrite phase which has an ordered layering structure described by Ustinovshchikov.

Flexural testing was done on cylindrical samples wherein the sample undergoes a 3 point bend. In a 3-point bend test, the sample rests on two supports a known distance apart, and a single point exerts force from above, creating torsional stress along the length of the sample. The bottom edge of the sample experiences tensile stress while the upper edge experiences compressive strength as the sample bends. This implies there exists an axis in the center of the sample that experience neither compressive nor tensile stress; this is known as the neutral axis and it plays a key role in the calculations when determining the strength of the material. The ferrosilicon samples

were tested using an Instron universal tester, which measures the force applied (F) to the sample as well as the deflection distance (D) of the sample under the applied load. The graphs of F vs D was converted to stress-strain curves using the following equations,

$$\sigma = \frac{FL}{\pi r^3}$$

$$\epsilon = \frac{6Dd}{L^2}$$

where σ is the stress in MPa, F is the applied force in Newtons, L is the distance in mm between the lower supports in the experimental setup, r is the radius of the cylindrical sample in mm, ϵ is the strain of the sample, D is the displacement of the sample during testing measured in mm, and d is the diameter of the sample in mm.

Stress-strain curves can provide a multitude of information about the characteristics of the sample material. A typical stress-strain curve has an elastic deformation region in which the displacement from a load would return to zero should the load be removed, which is typically a straight line. If the load exceeds a certain stress, known as the yield strength, the material is then permanently deformed and will continue to deform under higher loads, but at a different ratio of load to deformation until reaching a maximum stress before rupturing , ie the ultimate strength. If a material is brittle, it will not yield and deform, but rather rupture. This rupturing can happen prior to the end of the elastic deformation region and thus, the highest stress reached is considered the ultimate strength rather than the yield strength since the sample did not yield. The slope of the elastic deformation gives information about the rigidity of the material. Higher slopes indicate higher loads required to displace the sample, indicating rigid samples. This information is encapsulated in the flexural modulus, which is calculated by measuring the slope of the stress-

strain graph. The plastic deformation region gives information about the strength, toughness and ductility. The two types of strength of interest are the yield strength and ultimate strength, which are the point at which the elastic deformation ends and the point at which the sample is under peak stress, respectively. Similar to the measurement of the flexural modulus, a slope of the curve in the plastic deformation region can give info about the ductility; lower slopes indicate less force required to displace the material and hence are more ductile. The toughness is a measurement of the total energy required to break the material. The toughness goes down with increasing dislocations and voids, making the bulk of the material closer to an energy level required to make a new surface and breaking the material into pieces.

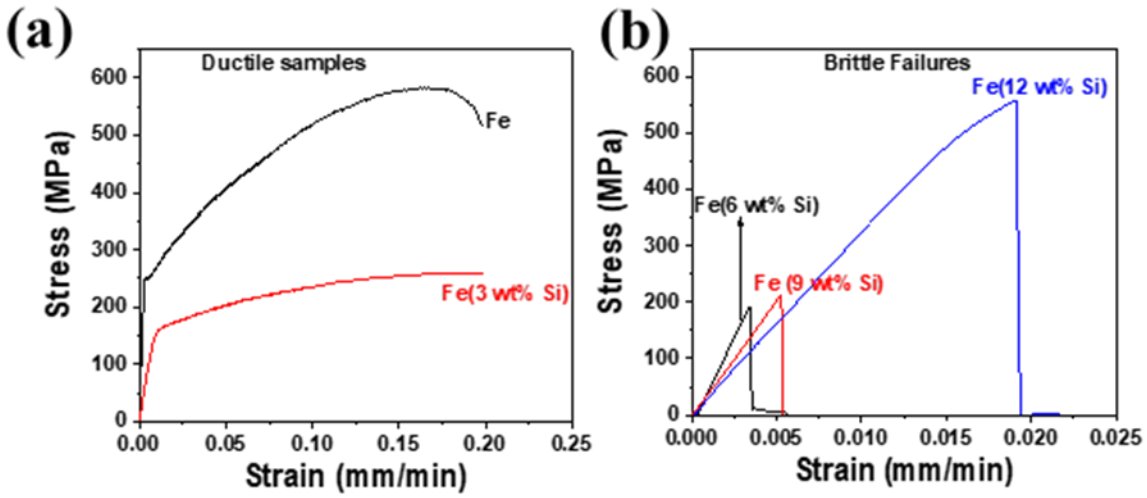

Figure 22: Stress-Strain curves for ferrosilicon samples. Samples with 3 wt% Si or less (a) showed enough ductility to enter the plastic deformation region without rupturing. The pure iron samples showed a much higher ultimate strength and yield strength compared to the 3 wt% Si sample. Samples with 6 wt% Si or more (b) were extremely brittle and ruptured without plastic deformation. Of the brittle samples, the 12 wt% Si samples showed a dramatic increase in

strength compared to the 6 and 9 wt% Si samples.

The ferrite microstructures in the lower silicon content samples allowed for enough ductility to plastically deform during the 3-point bend test. The ductility of the rods showed a dramatic decrease from 3 wt% to 6 wt%. The pure samples and the Fe(3 wt% Si) samples showed ductile nature and remained intact beyond the elastic region of the stress-strain curve, while the samples with 6 wt% Si or greater ruptured prior to the plastic deformation region. A representative stress-strain curve for each sample is shown in figure 22. The graphs are separated into ductile samples (a) and brittle samples (b). Of the ductile samples, the pure iron material showed a much higher yield strength (200 MPa) and ultimate strength (580 MPa) compared to the Fe(3wt% Si) sample which had a yield strength and ultimate strength of 153 and 232 MPa, respectively. The large area under the stress-strain curves of iron and Fe(3 wt% Si) sample indicate a tough material, which is advantageous for structural applications, whereas the Fe alloys with 6,9 and 12 wt% Si are very weak, meaning the total energy needed to disrupt the continuity of grains in the microstructure is relatively low, leading to a very brittle material. When comparing iron and the Fe(3 wt% Si) alloy, the iron is much more rigid as shown by the slope of the elastic deformation section of the stress-strain curve, and it is relatively strong. The Fe(3 wt% Si) samples, however, showed much higher ductility in the plastic deformation region from the small slope after the yield point. This is very advantageous when drawing a material into a wire which will be necessary to become a 3D printing feedstock. The Fe(3 wt% Si) alloy also has a relatively high strength compared to the samples with 6 and 9 wt% Si. This makes Fe(3 wt% Si) a strong potential candidate to be a feedstock material for off-world metal 3D printing. Of the brittle samples, Fe(12 wt% Si) showed the largest strength before rupturing, which was comparable to that of pure iron,

but showed extremely low strain during the elastic deformation before rupturing. Fe(6 wt% Si) and Fe(9 wt% Si) ruptured at much lower stress than the higher silicon content samples, making them both rigid, weak and brittle. While the ductility of ferrosilicon seems to end at some point between 3 wt% and 6 wt% Si, the ultimate strength of the materials at compositions of 12 wt% Si or higher suggest utility for these materials in applications other than wire-drawing and 3D printing. The flexural strength measurements are shown in figure 23. Since ferrosilicon alloys with 6,9 and 12 wt% Si did not yield, the stress at which the samples ruptured are considered the ultimate strength.

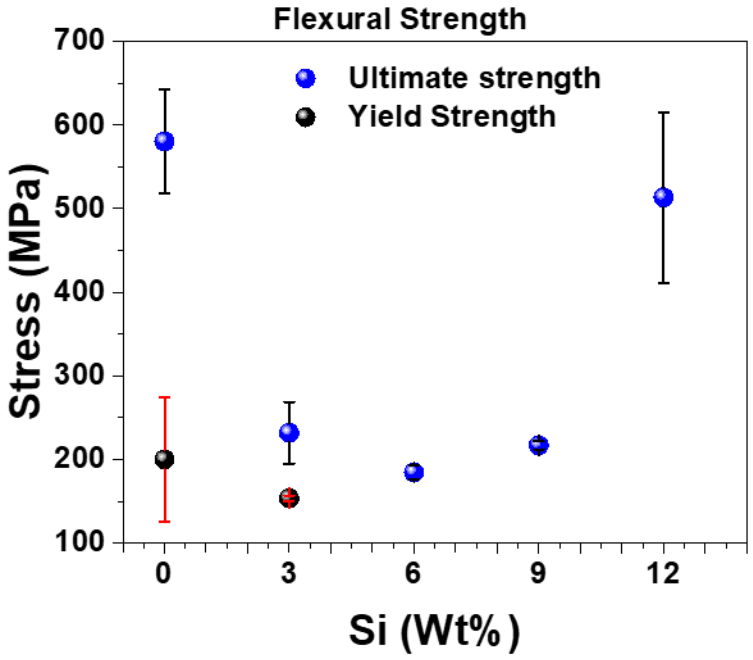

Figure 23: Flexural strength of ferrosilicon samples. Samples with 3 wt% Si or less experienced plastic deformation, thus, the yield strength and ultimate strength are both plotted whereas the samples with 6 wt% Si or more did not yield and therefore have no yield strength. The strength of the samples decreases until it hits a minimum around 6 wt% Si and then begins to increase

again as silicon content rises

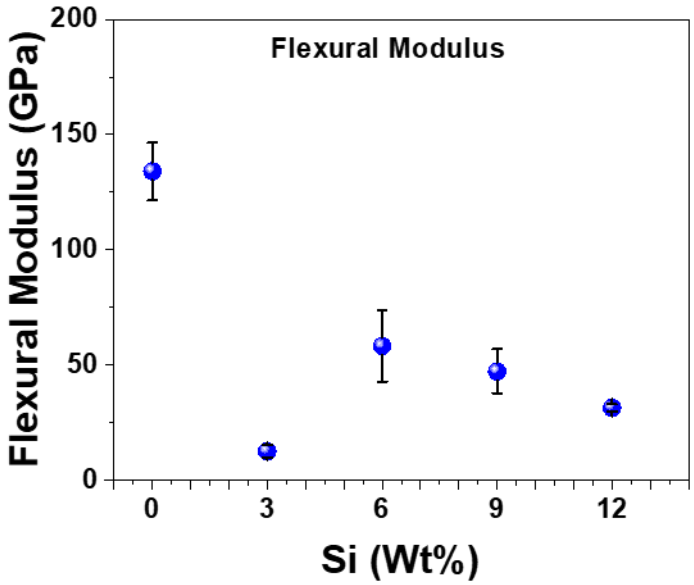

Figure 24: Flexural modulus of ferrosilicon samples. The modulus is dramatically lower for 3 wt% Si compared to the pure iron, making the 3 wt% Si much more ductile. The ferrosilicon samples with 6 wt% Si or more also had lower flexural modulus but ruptured very easily.

The flexural modulus of the samples is the ratio of stress to strain during the elastic deformation region. Graphically, this is the initial slope of the stress-strain curve. The calculated flexural modulus is also shown in figure 24. The flexural modulus, which is equivalent to the Young's modulus for isotropic materials drops dramatically from the pure iron sample to the Fe(3 wt% Si) alloy, making Fe (3 wt% Si) more ideal for drawing wire than the pure iron sample. The measured flexural modulus for Fe alloys with 6, 9 and 12 wt% Si are also considerably lower than the pure iron due to the low stresses applied before rupturing. While the slope of the stress-strain curve are favorable for drawing wire, the low ultimate strength and brittle nature make the

Fe(6 wt% Si) and higher samples less than ideal for 3D printing. The Fe(3 wt% Si) sample, while having lower ultimate and yield strength compared to the pure iron, is much more ductile and presents a good option for drawing wire as a 3D printing feedstock.

The design concepts for a wire-based 3D printer are either to melt a wire and mechanically feed the molten metal through a nozzle or to deposit material with an electrical arc similar to a welding process. For a welding technique to work, the electrical properties of the material must be well understood, particularly the resistivity of the material. The resistivity of the ferrosilicon ingots was measured and plotted in figure 25. The accepted value of the resistivity of iron was added to the plot for comparison[71] . An upward trend in the resistivity with increasing silicon content was expected since silicon has a much higher electrical resistivity than iron. The Fe(6 wt% Si) sample shows an unusually high resistivity, which can be the result of the solid mixture of different phases formed from the material cooling through the α2 phase and forming islands of B2 phase that α2 that act as electrical barriers. Since the welding process requires a completed circuit, the ideal material is a good conductor of electricity. Poor conduction in the welding circuit results in gaps in the weld leading to poor mechanical properties or failure. With a positive correlation between resistivity and silicon content, it is important to identify the maximum tolerable resistivity when designing a 3D printer for use with regolith-derived material. The resistivity measurements along with the measurements and error of strengths and compositions of synthesized materials are summarized in Table 5.

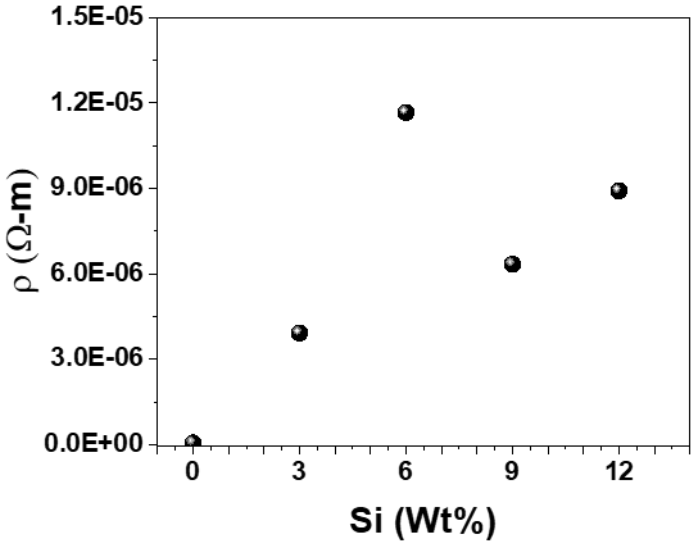

Figure 25: Resistivity measurements for ferrosilicon samples. The general upward trend with increasing silicon content is expected with silicon acting as a semiconductor. The Fe(6 wt% Si) data point is likely due to the inhomogeneous phase creation during the cooling.

Table 5: Summary of mechanical and electrical data collected on samples.

Target Composition	Measured Si Wt%	ρ(Ω-m)	ρ error (Ω-m)	Yield Strength (Mpa)	Ultimate Strength (Mpa)	Flexural Modulus (Gpa)
Fe	0	8.57E-8	Accepted Value	200.0 +/- 73.8	580.5 +/- 61.7	134.1 +/- 62.5
Fe(3 wt% Si)	2.84 +/- 0.8	3.92E-6	2.6E-8	153.7 +/- 3.4	232.0 +/- 36.9	12.5 +/- 2.7
Fe(6 wt% Si)	6.15 +/- 0.1	1.17E-5	5.7E-8	N/A	184.5 +/- 9.0	58.3 +/- 15.4
Fe(9 wt% Si)	9.22 +/- 1.6	6.34E-6	2.8E-8	N/A	217.0 +/- 4.8	47.3 +/- 9.6
Fe(12 wt% Si)	12.36 +/- 0.4	8.91E-6	3.5E-8	N/A	513.5 +/- 10.2	32.4 +/- 1.6

3.3 Advances in MRE technology

The MRE reactor to produce oxygen and metals from regolith powder remains at a low technology readiness level (TRL). Experiments have been performed to electrolyze simulated regolith, however the design of the reactor and the material selection of the electrodes lead to "catastrophic failure" as the ceramic walls of the reactor were eroded within an hour, or the electrode itself was eroded by the molten iron in the regolith [37]. Other future design requirements include an extraction device for metals, capture device for the gaseous oxygen and a starter device for the electrolysis reactor. To prevent rapid corrosion of the inner walls of the reactor, it is proposed that the ideal method of heating the regolith is from the center of the reactor outward via joule-heating from the electrical current of the electrodes. The electrical resistivity of the regolith can convert electrical energy from the electrodes into enough heat to keep the regolith above the melting point. The problem with this approach is the requirement that the regolith be in the molten state prior to the initiation of the joule-heating. Since electrical current cannot happen through the solid regolith, the powder must first be melted prior to both electrolysis and joule-heating. This section discusses experimental concepts to solve this issue of the initial melting of regolith in an MRE reactor.

Two methods of solving this issue have been studied. One method is to have a resistive heating element embedded in the regolith between the two electrodes, with a circuit in the reactor dedicated to this starter device. The heating element (most likely a wire, rod, or set or wires in parallel) would be overrun with current to heat the elements up beyond their melting point, which is well beyond the melting point of the surrounding regolith. This would make the heating element a sacrificial starter device for the MRE reactor, however, the aim is to use a metal that

can be produced from the MRE reaction, making it self-sustaining system. The main concern with this approach is the geometry of the source of heat, as the resulting pool of molten regolith would mimic the shape of the heater. For this reason, a thicker wire is ideal for making a wide molten pool, however a thicker wire will require much more current to produce heat.

Another method of melting regolith is magnetic induction. By matching the fluctuations of a magnetic field to the resonant frequency of a metal, the metal will begin to heat up. This method shows a lot of promise in non-contact forms of melting regolith and would represent a large increase in the technology readiness level of the MRE reactor. Magnetic induction as a means of melting regolith was tested by varying the heating parameters and metal shapes. For this study, a crucible of regolith simulant JSC-1A was placed in the center of an induction coil (figure 26), with a metal susceptor in the crucible to act as an internal heater to melt the regolith. A tall ceramic crucible is placed in the center of an induction coiled made of a 5/16” copper tube turned 3 times around the crucible forming a 3.2” inner diameter circle. The copper tubing is connected to the RDO induction power supply DuraPower 10-80 model, 10 kW, 20 kHz-80kHz. For this experimental test, three susceptor styles were chosen to try to achieve regolith melting; iron pellets, a steel coin and steel tubing.

Figure 26: Ceramic crucible inside RDO induction coil.

The iron pellets were first tested one at a time, embedded in regolith simulant. Despite varied power input (2 to 7.5 kW) the pellets did not melt but did glow. Then several pellets were placed in the regolith in such a way that the pellets were in electrical contact with each other. This allows Eddie currents formed within the bulk of the material to flow. At 7.5 kW, the pellets began to glow and partially, but not fully melt together. The iron pellets are shown in figure 27.

Figure 27: iron pellets before (left) and after (right) induction heating.

Since the pellets did not prove to be a suitable method for achieving the goal of melting the surrounding regolith, a steel coin was studied. The 1.25” diameter, 0.035” thick coin was embedded coaxially with the induction coil to allow for coupling of the metal with the magnetic

field. Within 20 seconds of the induction coil reaching 7.5 kW at 3.5 kHz, the coin began melting in various spots. Figure 28 shows the experiment setup as well as the partially melted coin. An interesting phenomenon occurred with the steel coin in which Eddie currents, that are present throughout the coin when influenced by a changing magnetic field, are concentrated at locations where melting has occurred. This results in faster heat propagation at that location and faster melting. The melting tends toward the center of the coin and can be seen in several locations on the coin. The coin melted much better than the pellets because the shape lent itself to easier coupling with the magnetic field. While the coin achieved melting, utilizing a coin shape is not ideal for use in an MRE reactor because the shape would lead to a molten pool of regolith that extends horizontally when the pool needs to reach both electrodes in a reactor, which are stacked vertically.

Figure 28: Induction heating of steel coin (left) and partially melted steel coin (right). The coin begins melting at the edge, causing a concentration of Eddie currents where the melting begins,

which further propagates the melting toward the center of the coin. This is seen in several locations on the coin.

After the coin, steel tubing was tested in the induction coil. A section of steel tube with 1" inner diameter, 1/8" wall thickness and 1" height was buried halfway with regolith. The induction coil was brought to 7.5 kW and 3.5 kHz. Within 2 minutes, the regolith began melting. More regoith was poured on the uncovered portion of the steel tube section, which resulted in melting of the new regolith. A progression of the test is shown in figure 29.

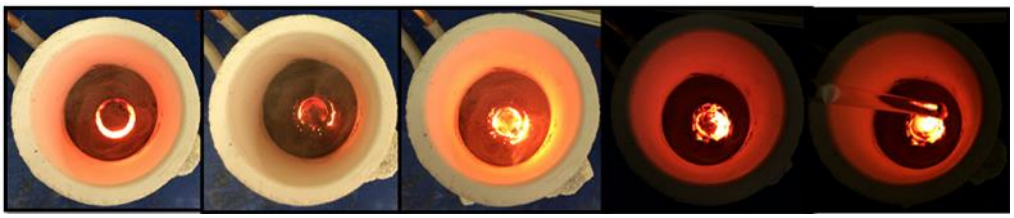

Figure 29: Progression of regolith melting via induction heating of steel tube.

Regolith inside the tube melted entirely and portions of the regolith outside the tube also melted. This sampled was recovered and imaged in figure 30 and figure 31. Figure 31 shows an image of the cross section of the cylindrical sample that developed a large crack down the height of the sample during the induction heating process. The figures also shows the solidified regolith bonded to the inside edge of the cylinder after being melted and re-solidified.

Figure 30: Steel tube section coated in regolith after melting in induction heater.

Figure 31: Optical image of steel susceptor for induction heating of regolith powder. The disconnect at the top of the image is from the metal piece melting. Glassified regolith can be seen inside the inner edge of the cross section which indicates the regolith reach melting temperatures at some point during the heating process.

The advantage of using this tube sample as a potential heat source in an MRE reactor is that the resulting pool of regolith will span the entire height of the tube, making it possible to melt regolith from one electrode to another in the center of the MRE reactor. This process will make it possible to simplify the MRE reactor design and to a “cold-walled” reactor; one in which molten

regolith will not contact with the inner walls of the reactor. This design concept prevents corrosion from the molten iron in regolith and centralizes the molten regolith to the zone between the electrodes.

CHAPTER FOUR: WIRE-BASED METAL 3D PRINTING

As technology progresses toward making humankind a space-faring species, arguably the most important capability is the on-demand production of specific goods and parts. Additive manufacturing promises to replace traditional manufacturing methods in favor of a bottom-up approach to production of specific parts. Printing parts with plastic or resin is a well understood technique and modern plastic 3D printers are common and inexpensive. In more recent years, a desire to print with metal has grown significantly and techniques for metal printing are becoming more mature. Most, however, rely on a bed of metal powder as a feedstock from which a pattern is selectively sintered into a solid piece. After a layer is completed, a new layer of powder is laid over the previous layer and the selective sintering process continues. This approach has many drawbacks, including the need to fill an entire printing bed to produce a part, leaving the vast majority of the feedstock unused. Another major problem with this printing technique is the use of powders, which will not transfer into in-space use as powders are extremely difficult to control in low and zero-gravity environments. For this reason, the development of a wire-based printing technique is needed and this study focuses on the characterization of the first metal part 3D printed from a wire. For this study, feedstock material was chosen based on metals that can be directly obtained from regolith powder via the MRE and other ISRU processes. Although carbon can be obtained from the atmosphere of the Mars, we chose a very low carbon steel to study for this process to minimize the carbon requirement for off-world applications. The steel that was used

also contains a relatively large proportion of silicon to accommodate the silicon that will be electrolyzed from the regolith along with iron in the MRE process. Although this chosen feedstock material has not yet been directly derived from regolith material in a laboratory setting, it serves as an adequate simulated version of the metals that can, one day, be derived from the martian environment from in-situ resource utilization processes.

4.1 Iron-Silicon printing

3D printing with metal has been in development with the majority of commercially available printers being powder-based. Current wire-based printers rely on an electron beam source, which are costly and difficult to maintain. Made in Space, Inc has developed a wire-based 3D printer using arc-based metal joining technique with3 degrees of freedom to perform multilayer free-form fabrication. All fabrication was done in an inert atmosphere under ambient temperature and pressure. Figure 32 shows the prototype wire-based 3D.

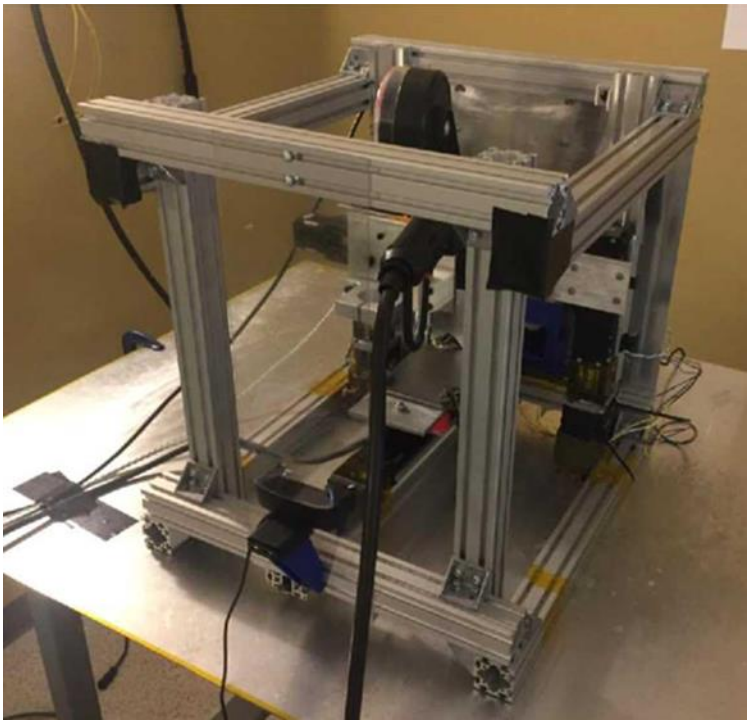

Figure 32: Benchtop metal additive manufacturing test unit.

Two types of feedstock wire were used for printing tests. A core-shell FeSi wire was fabricated and characterized prior to printing. The wire consisted of a powdered silicon core wrapped inside a low-carbon steel sheath. The elemental composition of the core-shell wire was measured by x-ray fluorescence and is shown in figure 33. The silicon content was 28 wt%.

Element	Concentration (wt %)
Fe	71.21
Si	28
Mn	0.22
Cr	0.2
Al	0.08
Ti	0.08
.Sn	0.06
C	0.056
Cu	0.03
Nb	0.02
P	0.015
S	0.013
Ni	0.01
V	0.01
Co	< 0.01
Mo	< 0.01
W	< 0.01
Zr	< 0.01
B	< 0.001

Figure 33: elemental composition of the experimental core-shell iron silicon wire as measured by X-ray florescence.

This experimental wire was very stiff and could not be accommodated into the feeder system, so small segments of the wire were cut and fed individually into the print head. The printed ferrosilicon parts showed minimal luster as compared to previously made iron and a large amount of sputtering occurred on the build plate. The resultant printed pieces, shown in figure 34, were very brittle and broke during removal from the build plate. These samples were examined under an optical microscope to reveal a very porous core to the printed part, likely a result of the high concentration of silicon powder in the core of the wire.

Figure 34: Build plate with 3D printed parts from experimental core-shell iron silicon wire

The electrical current used in the printing process likely traveled through the steel shell of the wire as that material has a much higher electrical conductivity. This resulted in uneven ejection of material from the wire and an incomplete melting of the silicon core. Figure 35 below shows the cross section of a part from this experiment.

Figure 35: Optical image of the cross section of printed part from experimental core-shell iron-silicon wire.

4.2 ER70S-6 Welding Wire as 3D printing Feedstock

Sample preparation from a welding wire feedstock was performed using the novel additive manufacturing (AM) system that performs arc-based metal joining. The system has 3 degrees of

freedom to perform multilayer free-form fabrication. An inert 100% argon gas was used for all tests to operate the machine under ambient atmosphere and temperature. The MIS Metal-AM system, feeds wire into a MIG welder and is controlled to move around a cartesian gantry to weld material in a controlled pattern. During sample preparation, fabrication parameters were selected by varying travel speed, wire speed, voltage and gas flow rate. The working distance between the tool head and the substrate was maintained at 10mm. A 6.35mm thick low carbon steel substrate was used as a build plate for all tests and the feedstock material (0.6mm ER70S-6 welding wire) was deposited on the substrate via an arc-welding process. Two samples were manufactured for mechanical testing by stacking a single row of material for eight layers for sample 1 (Figure 36a) and 20+ layers for the second printed sample (Figure 36b). These samples were cut by an electric discharge machine (EDM) into rectangular pieces for 3-point bend testing. Figure 36c, and 36d show the directions of the cuts made on the printed pieces.

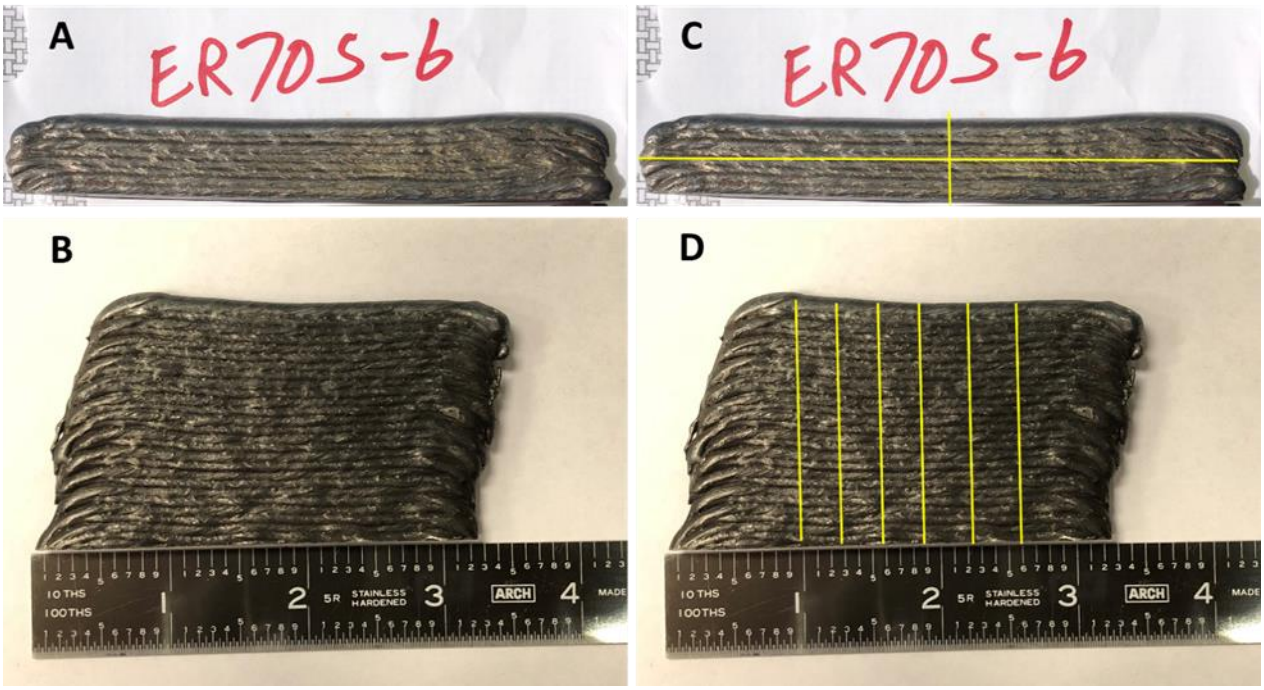

Figure 36: Metal pieces printed from ER70s-6 welding wire 0.6mm feedstock. The first printed sample (a) was welding onto the steel build plate with each layer stacked vertically on top of subsequent layer, totaling 8 layers. The second sample (b) was made in the same manner with over 20 layers stacked. The samples were cut along the yellow lines (c,d) by an EDM machine to then be tested in the Instron 3-point bend test.

These cuts were made such that every possibility of directionality of the printed layers relative to the direction of applied force of the 3-point bend tester is represented. Figure 37 describes the directionality of the pieces in the 3-point bend test and how each samples were labeled. The sample labeled S1-Y is the piece cut from sample 1 (S1) where the printed layers, if imagined as flat 2 dimensional planes, are lying on the XZ plane as defined by the labeled axes in figure 37 and moving from one layer to an adjacent layer is a movement in the Y direction. This convention is extended to the other samples; the S1-Z sample is made from sample 1 and is

oriented such that layers are stacked in the Z direction. Sample S2-X was cut from the second printed part and was positioned in the 3-point bend tester such that layers are adjacent in the x direction. The bend test was done using an Instron universal tester. After bend the samples were cast in resin and polished using 0.1 µm alumina slurry and etched using 2% natal etchant before imaged using an Olympus GX71 optical microscope and Keyence optical microscope.

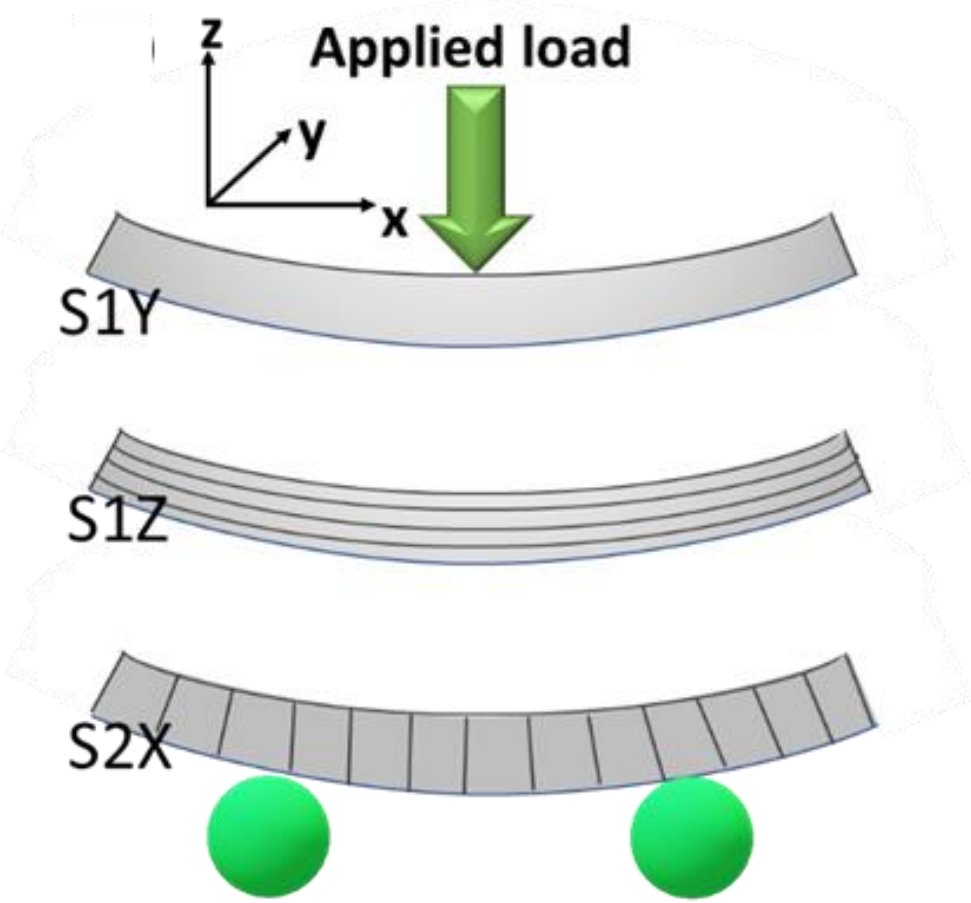

Figure 37: Diagram of 3-point bend test with directionality of samples relative to the applied load. The lines in the samples represent junctions between layers

The stress-strain curves for the three sets of samples are shown in figure 38. S2-X and S1-

Z show similar characteristics as each other while S1-Y appears to be considerably weaker than the previous two. S2-X and S1-Z have very similar yield strengths (548 MPa and 530 MPa, respectively) but S2-X showed an ultimate strength of 1028 MPa while the ultimate strength of S1-Z was measured to be 836 MPa. S1-Y showed much weaker mechanical properties with a yield strength and ultimate strength of only 329 MPa and 648 MPa, respectively. The flexural modulus for S1-Y, S1-Z and S2-X follows the same general trend as the ultimate strength with values of 8.6 GPa, 11.8 GPa and 22.9 GPa, respectively. The measured flexural modulus for this part is not necessarily equal to the elastic modulus for a casted mild steel of the same composition due to the anisotropic nature of the printing process. Literature [71] on mild steels reports the yield strength of the cast material at 360 MPa, which is directly in line with our measurement of S1-Y. S1-Z, which was cut from the same printed part as S1-Y, showed a much higher yield strength and ultimate strength than the S1-Y samples. These measured values are summarized in Table 6. Sample 2 also showed an elevated strength from S1-Y and can be explained with an examination of the microstructure of the printed parts.

Polished and etched samples of the printed part were initially examined using a Keyence optical microscope to view the microstructure of the part's cross section. Figure 39 shows the etched cross section with an edge of the sample exposed to see the topography of the junction between adjacent layers. The etching exposed a pattern of dark bands extending the width of the cross section that appeared to originate at the junction between layers. A more thorough examination of the microstructure was done with an Olympus optical microscope and SEM. Figure 41a shows a low-magnification optical image confirming the banded pattern of the microstructure of the sample and figure 41b is a high-magnification image from the same area of

the sample. In figure 41b, it can be seen that the banded dark areas have large portions of a cementite phase present and the light areas are a predominantly ferrite structure. These bands of patterned microstructures form in a shape that can be expected from the welding process. Every welding process produces a “heat affected zone” (HAZ) on the welded piece which can change the microstructure of the base metal [72,73]. This phenomenon is usually characterized by larger grains of ferrite, with fewer cementite islands and is diminished as the distance from the weld increases due to the thermal gradient and cooling rate.

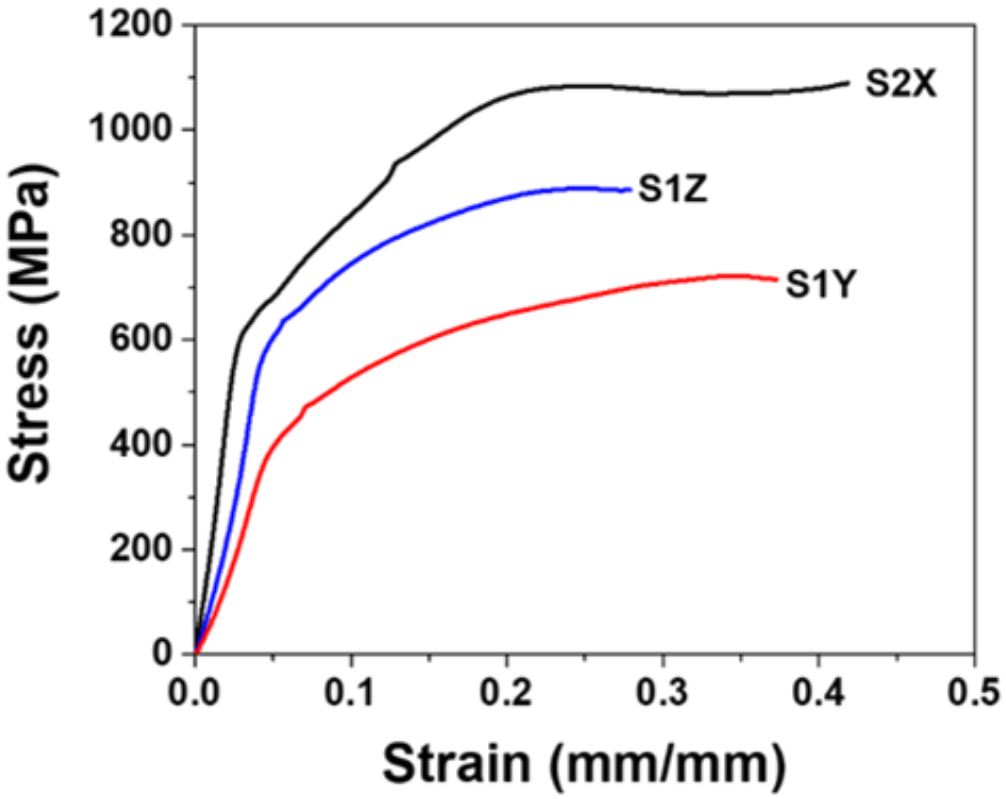

Figure 38: Stress-Strain curves from 3-point bend test of printed samples. S1-Z and S2-X showed very similar yield strength (530 MPa) but differed slightly with ultimate strength and flexural modulus. S2-X and S1-Z had an ultimate strength of 1028 MPa and 836 MPa, respectively, and a

flexural modulus of 22.9 GPa and 11.8 GPa, respectively. S1-Y showed much lower yield strength (330 MPa), ultimate strength (648 MPa) and flexural modulus (8.6 GPa) compared to S1-Z and S2-X

With each successive pass of the welding process, the previous layer develops a HAZ causing grain coarsening, and an apparent change in coloration in the shape of an arc across the cross section of the sample. Coarse grains impart ductility while smaller grains impart strength so the directionality of the macrostructure can give the part an anisotropic effect for the bending test.

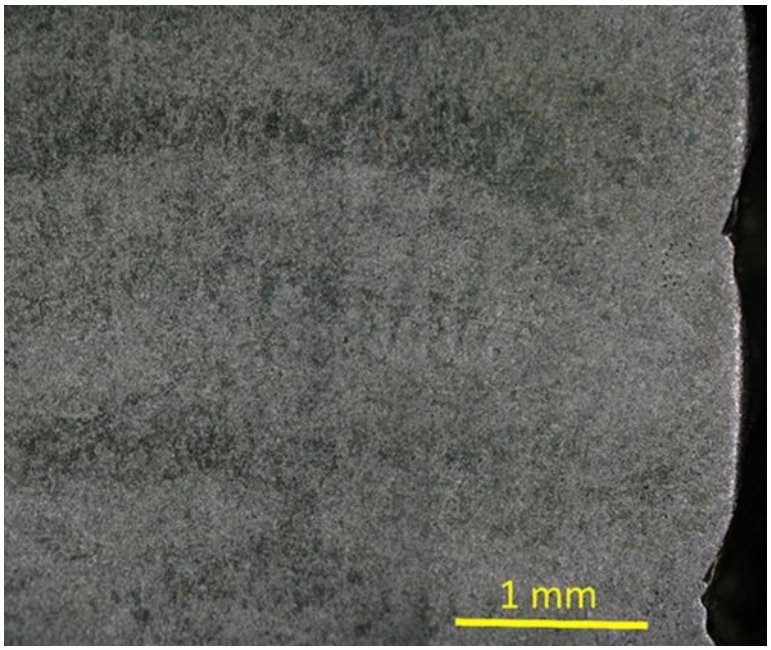

Figure 39: Optical image (Keyence) of etched cross section of 3D printed part. The right side of image has exposed side of the part and the uneven junction between layers can be seen. On the surface of the cross section, bands of discolored sections can be seen extending the width of the cross section

Kuerová et al [74] , performed a experimental study on the effect of volume fraction of bainite on the yield strength and ductility of steels. The prediction that the yield strength of the material increases with increasing bainite volume fraction was verified by experimental results. A similar study [75] was done by Schade et al, which demonstrates a direct correlation between the bainite volume fraction and the mechanical strength of the material. The majority of the bulk material in our printed part has bainitic concentrations, which impart high yield strength to the part. The larger ferrite grains in the HAZ of each layer also impart ductility to the sample. For the S1-Y sample, the bottom and top edges of the sample, where the maximum tension and compression forces are applied, have a large number of HAZ zones due to the layer junctions on the surfaces of the samples and these bands are oriented parallel to the applied stress. This is likely the reason the S1-Y sample showed a lower mechanical strength compared to the other sample orientations. The S1-Z and S2-X sample both had orientations that would have minimized the effects of the HAZ bands. S1-Z was cut in such a way that the upper and lower edges of the part were cut through the middle of layers, making the surfaces of the test part under the highest amount of stress lower grain size sections. S2-X, which did show a slightly lower yield strength than S1-Z, had HAZ sections at the edges but unless they were exactly under the applied load, the highest concentrations of stress were still experienced by regions of smaller grain concentrations. As this new technology develops, it may be possible to tailor the microstructure of the samples by maintaining a slower cooling rate or manipulating the rate at which new material is deposited. Research is still ongoing to develop this technology for other metals that

can be produced from the local environments on a lunar of Martian colony.

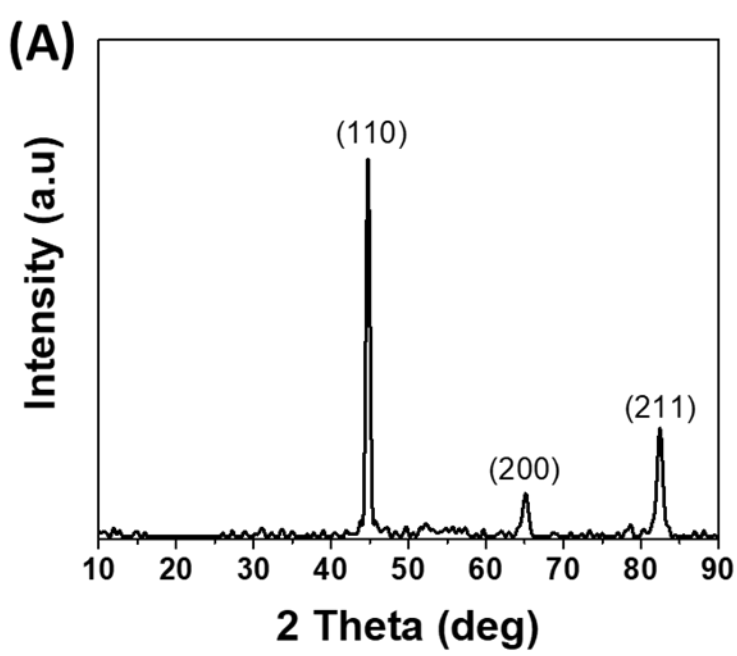

(C) EDS result

	Wt %	Error (+/-)
Fe	95.97	1.59
Mn	1.40	0.18
Si	0.89	0.27
O	1.81	1.33

Figure 40: (A) XRD spectrum of powdered 3D printed samples showing BCC structure of mild steel. (B) SEM image of the powdered 3D printed samples and corresponding EDS results in (C).

Sections of the printed samples were powdered by cutting with a diamond blade to produce enough material to perform X-ray diffraction (XRD) and Energy-dispersive X-ray spectroscopy (EDS) to confirm composition and phases present. X-ray diffraction (XRD) analysis on the sample showed a classic BCC structure with peak positions corresponding to the (110), (200), and (211) planes of ferritic steel. The XRD data is shown in figure 40a. Also notable in the XRD data is a lack of peaks belonging to any cementite crystal structure when considering steel. Although the microstructure of the steel (discussed below) shows an upper bainite structure, the very low carbon content of the material makes it impossible to have formed enough cementite to be detected by XRD. This is the case with many other publications [72,73]. The sample was

cooled via conduction with the argon atmosphere and the temperature of the sample was measured via IR camera. After deposition of a layer, the temperature of the fresh layer was measured at 300°C within 2-3 seconds after deposition. This cooling rate is too slow to have formed martensite and therefore likely to have formed bainite, or possibly some pearlite. SEM and EDS data in figure 40b,c shows this steel is alloyed with manganese and silicon and has minimal oxidation. These samples were made from ER70S-6 mild steel, which is typically composed of manganese between 1.40 and 1.85 wt%, silicon between 0.80 and 1.15 wt% and carbon between 0.06 and 0.015 wt% with trace amounts of other elements. Figure 41c,d shows colonies of bainite structure from the etched cross section of the sample. The EDS data of the printed sample are in agreements with the composition range of the feedstock material. This structure of welded steel makes the otherwise solid, voidless part anisotropic and thus the bend testing that was performed is expected

to have differences based on the directionality of the part relative to the exerted stresses.

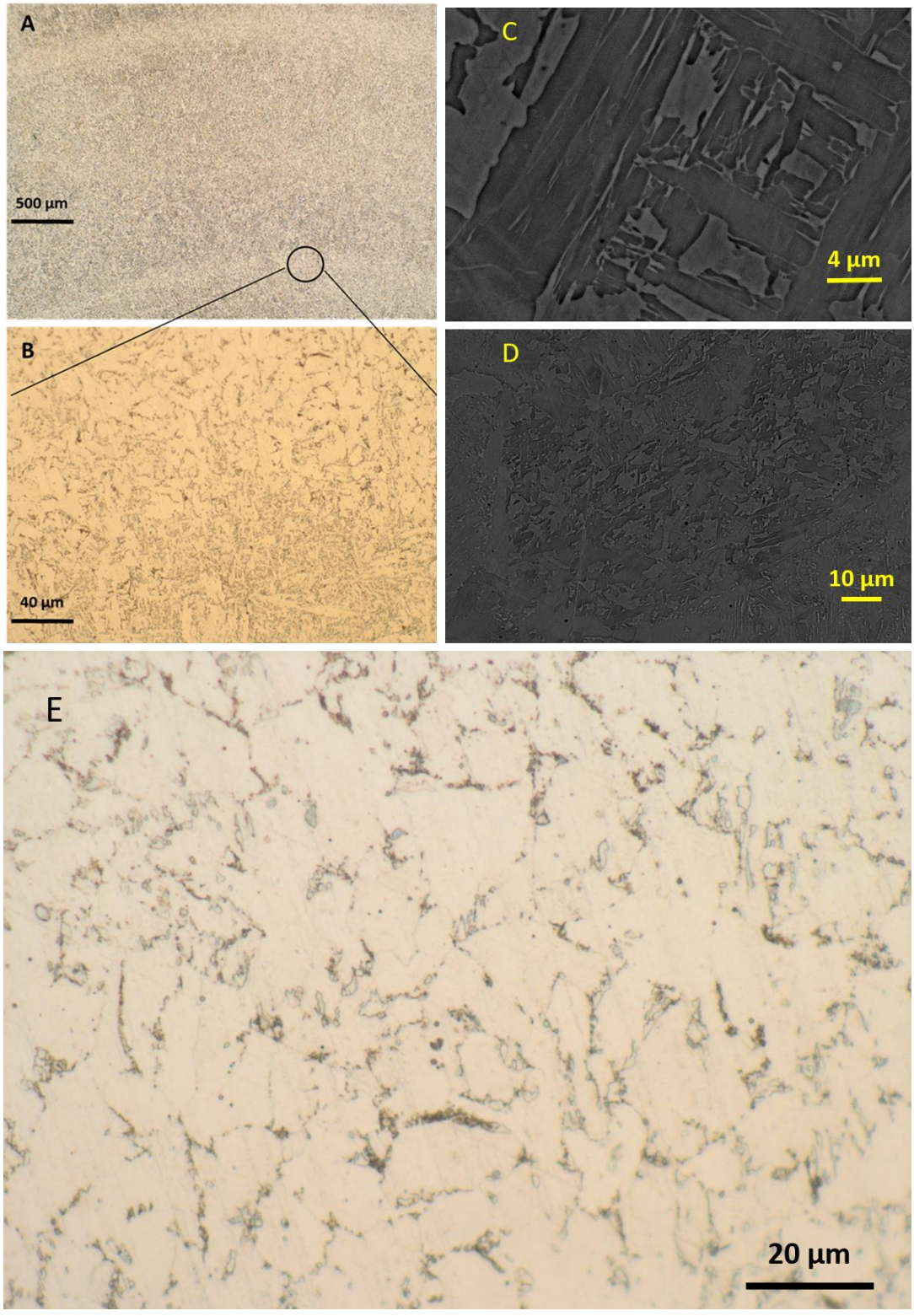

Figure 41: (a,b)Optical image (Olympus) of etched cross section of 3D printed part. The low-magnification image (a) shows bands of lighter areas in the microstructure near the top and bottom of the image. These bands of light colored areas extend across the width of the sample and reach a maximum near the middle of the sample. The low-magnification image (b) is of an area near the edge of the light band and exposes the difference in coloration and microstructure associated with HAZ zones from welding. (c,d) SEM images of etched surface of printed sample. Colonies of large upper bainite structures are shown. (e) optical image of bright area of polished smaple

Table 6: Summary of Mechanical Properties of ferrosilicon alloy samples.

Sample	Yield Strength (MPa)	Ultimate Strength (MPa)	Flexural Modulus (GPa)
S1-Y	329 +/- 52	648 +/- 107	8.6 +/- 0.8
S1-Z	530 +/- 31	836 +/- 75	11.8 +/- 0.4
S2-X	529 +/- 22	1028 +/- 39	22.9 +/- 3.4

CHAPTER FIVE: CONCLUSION

In this study of construction materials for lunar and Martian colonies, two separate applications were studied; sintering and 3D printing. Sintering objects such as bricks from regolith powder has the advantage of relying fully on materials ubiquitous in a colony on the moon or Mars. The sintering process requires only energy to heat the material, and the material itself. Although the sintering process is simple in operation, the properties of the final product of sintering depend heavily on the heating profile of the material including the maximum temperature and the hold time at maximum temperature. The sintering process also depends on the total surface area of the powder material since sintering is a process that occurs at the surface between adjacent particles. A study was done on lunar and Martian simulants in an attempt to determine optimal conditions for sintering bricks of high compressive strength. It was determined, intuitively so, that the highest strength bricks were made from material of the smallest particle size range and largest sintering temperature without melting the material. Samples of JSC-1A lunar simulant were melted and the re-solidified material became glassy and extremely brittle. The mechanical strength of the sintered bricks has a strong correlation with the volume % of voids within the bulk of the brick. The smallest particle size samples showed a void volume % of less than 0.5 vol % and a mechanical strength of 38,000 psi; over 10 times higher than Portland cement.

An examination of the use of additive manufacturing in space colonies highlights it as an ideal technology to implement for both small-scale manufacturing and large-scale construction applications. A large effort to develop wire-based additive manufacturing techniques for space colonies is underway with collaboration with NASA and commercial entities. Automated additive manufacturing techniques for colonization applications provides the advantage of eliminating the need to ship parts that could be printed on site. Parallel efforts are focused on developing a feedstock material that can be derived from regolith powder. This development eliminates the need to ship printing material from earth, making the process of printing parts or buildings an almost completely zero mass launch process.

To this end, the material products of molten regolith electrolysis, ferrosilicon alloy, were examined for their mechanical and electrical properties with the goal of identifying an alloy that can be used as a feedstock material for 3D printing technologies. It was found that material below 3 wt% Si in iron were ductile enough to yield to stresses rather than rupture and were also strong enough to be used for mechanical purposes. The material in the low-silicon end of the composition spectrum also showed the lowest electrical resistivity, making this ideal for a welding additive manufacturing technique.

A 3D printing technique for wire-based 3D printing has been studied and metal parts printed from this novel technique have been fully characterized. Made in Space Inc has built a 3D printer from a MIG welder that takes in 0.6mm welding wire as a feedstock and arc welds material to a steel build plate. The advantage of the wire feedstock system is its capability to operate in low and zero gravity environments. Parts printed from this process were found to have patterned formations of low-pearlite areas at the junction between adjacent layers from the rapid

cooling of newly printed layers. These junctions between layers impart low yield strength when bent in one of the three possible directions from the 3-point bend test. The printed parts were otherwise found to have very high yield strength and ultimate strength.

These developments in construction material are the subject of ongoing research and represent a large advancement toward the capability of humans to live and thrive on the surface of another planet.

LIST OF REFERENCES

[1] John, W., & Arthur, W. (1990). Low-Cost Design Approaches for Earth-to-Orbit Propulsion. SAE Transactions, 187.

[2] McCleskey, C. M., Zapata, E., & Rhodes, R. E. (2014). An Analysis and Review of Measures and Relationships in Space Transportation Affordability. In 50th AIAA/ASME/SAE/ASEE Joint Propulsion Conference (p. 3649).

[3] Felisa Córdova, G., & Pablo González, A. (2017). The 'Mission to Mars' Case Study, Galbraith's Star Model and other Relevant Organization Theory, Critically Evaluate the Reorganization of the Mars Programme that Resulted from the Introduction of the 'Faster, Better, Cheaper' Approach at NASA. Journal Of Systemics, Cybernetics And Informatics, Vol 15, Iss 3, Pp 66-69 (2017), (3), 66.

[4] https://www.cnbc.com/2016/06/02/musk-we-intend-to-launch-people-to-mars-in-2024.html

[5] NASA's Space Launch System : powering the future of exploration. (2013). [Huntsville, Ala.] : National Aeronautics and Space Administration, [Marshall Space Flight Center], [2013].

[6] Frydenvang, J., Beck, P., Maurice, S., Gasnault, O., Rapin, W., Forni, O., & ... Ollila, A. M. (2016). ChemCam activities and discoveries during the nominal mission of the Mars Science Laboratory in Gale crater, Mars. Journal Of Analytical Atomic Spectrometry, 31(4), 863-889.

[7] Liu, Y. l., Goudge, T. A., Catalano, J. G., & Wang, A. (2018). Spectral and stratigraphic mapping of hydrated minerals associated with interior layered deposits near the southern wall of Melas Chasma, Mars. Icarus, 30262-79.

[8] Mixing relationships in the Martian regolith and the composition of globally homogeneous

dust. (n.d). GEOCHIMICA ET COSMOCHIMICA ACTA, 64(12), 2155-2166.

[9] Modeled Martian subsurface elemental composition measurements with the Probing In situ with Neutron and Gamma ray instrument: Gamma and Neutron Measurements on Mars. (2017). doi:10.1002/2016EA000162

[10] Wittmann, A., Korotev, R. L., Jolliff, B. L., Irving, A. J., Moser, D. E., Barker, I., & Rumble, D. (2015). Petrography and composition of Martian regolith breccia meteorite Northwest Africa 7475. Meteoritics & Planetary Science, (2), 326. doi:10.1111/maps.12425

[11] READ, P. L., LEWIS, S. R., & KASS, D. M. (2017). THE STATE OF THE MARTIAN CLIMATE. Bulletin Of The American Meteorological Society, 98(8), S60-S62.

[12] Chang, Y., Yin, Q., Lu, Z., Chang, Y. C., Ng, C. Y., Jackson, W. M., & Yin, Q. (n.d). Evidence for direct molecular oxygen production in CO2 photodissociation. Science, 346(6205), 61-64.

[13] New metal-organic framework turns CO2 into methane. (2017). TCE: The Chemical Engineer, (913/914), 23.

[14] Sunyhik Ahn et al, Poly-Amide Modified Copper Foam Electrodes for Enhanced Electrochemical Reduction of Carbon Dioxide, ACS Catalysis (2018).

[15] Diez, A. (2018). Liquid water on Mars. Science (New York, N.Y.), 361(6401), 448-449. doi:10.1126/science.aau1829

[16] Orosei, R. r., Lauro, S. E., Pettinelli, E., Cicchetti, A., Coradini, M., Cosciotti, B., & ... Noschese, R. (2018). Radar evidence of subglacial liquid water on Mars. Science, 361(6401), 490-493.

[17] THRYFT, A. R. (2013). NASA Working on Lunar Mining Robot. Design News, 68(6), M4.

[18] Direct evidence of surface exposed water ice in the lunar polar regions

Shuai Li, Paul G. Lucey, Ralph E. Milliken, Paul O. Hayne, Elizabeth Fisher, Jean-Pierre Williams, Dana M. Hurley, Richard C. Elphic

Proceedings of the National Academy of Sciences Aug 2018, 201802345; DOI: 10.1073/pnas.1802345115

[19] Kavan, L., Knizek, A., Zukalova, M., Kavan, L., Zukal, A., Kubelik, P., & ... Skrehot, P. (n.d). Spontaneous oxygen isotope exchange between carbon dioxide and natural clays: Refined rate constants referenced to TiO2 (anatase/rutile). Applied Clay Science, 1376-10.

[20] Junaedi, C., Hawley, K., Walsh, D., Roychoudhury, S., Abney, M., & Perry, J. (2011, July). Compact and lightweight sabatier reactor for carbon dioxide reduction. In 41st International Conference on Environmental Systems (p. 5033).

[21] Walton, O., Moor, C., & Gill, K. (2007). Effects of gravity on cohesive behavior of fine powders: implications for processing Lunar regolith. Granular Matter, 9(5), 353-363. doi:10.1007/s10035-006-0029-8

[22] Metzger, P., Britt, D., Covey, S., & Lewis, J. S. (2017, September). Figure of Merit for Asteroid Regolith Simulants. In European Planetary Science Congress (Vol. 11).

[23] Suescun-Florez, E., Suescun-Florez, E., Roslyakov, S., Iskander, M., & Baamer, M. (n.d). Geotechnical Properties of BP-1 Lunar Regolith Simulant. Journal Of Aerospace Engineering, 28(5),

[24] Hogue, M. et al."Regolith Derived Heat Shield for a Planetary Body Entry and Descent System with InSitu Fabrication", presentation to the 2012 NIAC Spring Symposium March 27-29, 2012

[25] Regolith Biological Shield for a Lunar Outpost from High Energy Solar Protons. (2008). doi:10.1063/1.2845005

[26] A FUTURE MARS ENVIRONMENT FOR SCIENCE AND EXPLORATION Planetary Science Vision 2050 Workshop 2017(LPI Contrib. No .198)

[27] Hobosyan, M. A., & Martirosyan, K. S. (2014). Consolidation of Lunar Regolith Simulant by Activated Thermite Reactions. Journal of Aerospace Engineering, 28(4), 04014105. [28] Jakus, A. E., Koube, K. D., Geisendorfer, N. R., & Shah, R. N. (2017). Robust and Elastic Lunar and Martian Structures from 3D-Printed Regolith Inks. Scientific Reports, 744931. doi:10.1038/srep44931

[28] Mueller, R. P., Howe, S., Kochmann, D., Ali, H., Andersen, C., Burgoyne, H., ... & Gerner, S. (2016, April). Automated additive construction (AAC) for Earth and space using in-situ resources. In Proceedings of the Fifteenth Biennial ASCE Aerospace Division International Conference on Engineering, Science, Construction, and Operations in Challenging Environments (Earth & Space 2016). American Society of Civil Engineers.

[29] Williams, R. J. (1985). Oxygen extraction from lunar materials: An experimental test of an ilmenite reduction process. In Lunar bases and space activities of the 21st century (p. 551).

[30] Christiansen, E. L., Simonds, C. H., & Fairchild, K. O. (1988). Conceptual design of a lunar oxygen pilot plant. In Second Conference on Lunar Bases and Space Activities of the 21st Century (Vol. 652, p. 52).

[31] B. Sherwood and G. R. Woodcock, “Cost and benefitsof lunar oxygen: Economics, engineering, and operations,” 1993. 1

[32] J. Diaz, B. Ruiz, B. Blair, M. Harsch, M. Duke, C. Parrish, D. Lueck,R. Mueller, J. Whitlow,

D. Boucher, K. Nock, P. Penzo, J. Sanders, S. Baird and K. Romig, “STARLITE -Space Transportation Architectures and Refueling for Lunar and Interplanetary Travel and Exploration,”NASA Grant NAG9-1535, Center forthe Commercial Applications of Combustion in Space, Colorado School of Mines, Golden, Colorado, June 5, 2005

[33] Joosten, B., & Guerra, L. (1993). Early lunar resource utilization-A key to human exploration. In Space Programs and Technologies Conference and Exhibit (p. 4784).

[34] Wang, D., Gmitter, A. J., & Sadoway, D. R. (2011). Production of oxygen gas and liquid metal by electrochemical decomposition of molten iron oxide. Journal of the Electrochemical Society, 158(6), E51-E54.

[35] Schreiner, S. S., Sibille, L., Dominguez, J. A., & Hoffman, J. A. (2016). A parametric sizing model for Molten Regolith Electrolysis reactors to produce oxygen on the Moon. Advances in Space Research, 57(7), 1585-1603.

[36] Schreiner, S. S. (2015). Molten Regolith Electrolysis reactor modeling and optimization of in-situ resource utilization systems (Doctoral dissertation, Massachusetts Institute of Technology).

[37] Sirk, A. H., Sibille, L., & Sadoway, D. R. (2010). Direct Electrolysis of Molten Lunar Regolith for the Production of Oxygen and Metals on the Moon

[38] Sibille, L., & Dominguez, J. (2012, January). Joule-heated molten regolith electrolysis reactor concepts for oxygen and metals production on the moon and mars. In 50th AIAA Aerospace Sciences Meeting including the New Horizons Forum and Aerospace Exposition (p. 639).

[39] Schwandt, C., Hamilton, J. A., Fray, D. J., & Crawford, I. A. (2012). The production of

oxygen and metal from lunar regolith. Planetary and Space Science, 74(1), 49-56.

[40] Schreiner, S., Sibille, L., Dominguez, J., Sirk, A., Hoffman, J., & Sanders, G. (2015). Development of a Molten Regolith Electrolysis Reactor Model for Lunar In-Situ Resource Utilization". In 8th Symposium on Space Resource Utilization (p. 1180).

[41] STOPAR, JD; et al. Relative depths of simple craters and the nature of the lunar regolith. ICARUS. 298, 34-48, ISSN: 00191035.

[42] Papike, J. J., S. B. Simon, and J. C. Laul (1982), The lunar regolith: Chemistry, mineralogy, and petrology, Rev. Geophys., 20(4), 761–826, doi:10.1029/RG020i004p00761

[43] Simon, S. B., J. J. Papike, and J. C. Laul (1982), The Apollo 14 Regolith: Petrology of cores 14210/14211 and 14220 and soils 14141, 14148, and 14149, J. Geophys. Res., 87(S01), A232–A246, doi:10.1029/JB087iS01p0A232.

[44] Papike, J. J., F. N. Hodges, A. E. Bence, M. Cameron, and J. M. Rhodes (1976), Mare basalts: Crystal chemistry, mineralogy, and petrology, Rev. Geophys., 14(4), 475–540, doi:10.1029/RG014i004p00475.

[45] Ray, C. S., Reis, S. T., Sen, S., & O'Dell, J. S. (2010). JSC-1A lunar soil simulant: Characterization, glass formation, and selected glass properties. Journal of Non-Crystalline Solids, 356(44-49), 2369-2374.

[46] Meurisse, A., Beltzung, J. C., Kolbe, M., Sperl, M., & Cowley, A. (n.d). Influence of Mineral Composition on Sintering Lunar Regolith. Journal Of Aerospace Engineering, 30(4)

[47] Bonanno, A. b., & Bernold, L. l. (2015). Exploratory Review of Sintered Lunar Soil Based on the Results of the Thermal Analysis of a Lunar Soil Simulant. Journal Of Aerospace Engineering, 28(4), 1-8.

[48] Lim, S., Anand, M., Prabhu, V. L., & Taylor, L. A. (n.d). Extra-terrestrial construction processes - Advancements, opportunities and challenges. Advances In Space Research, 60(7), 1413-1429.

[49] LI, F; PAN, J. Modelling „Nano-Effects" in Sintering. Sintering (9783642310089). 17, Jan. 2013. ISSN: 9783642310089.

[50] MEURISSE, A; et al. Influence of Mineral Composition on Sintering Lunar Regolith. Journal of Aerospace Engineering. 30, 4, 1-8, July 2017. ISSN: 08931321.

[51] TAYLOR, SL; et al. Sintering of micro-trusses created by extrusion-3D-printing of lunar regolith inks. Acta Astronautica. 143, 1-8, Feb. 1, 2018. ISSN: 0094-5765.

[52] TAYLOR, LA; MEEK, TT. Microwave Sintering of Lunar Soil: Properties, Theory, and Practice. Journal of Aerospace Engineering. 18, 3, 188-196, July 2005. ISSN: 08931321.

[53] Chen, W. (n.d). Comparison of ASTM saturation techniques for measuring the permeable porosity of concrete. Cement And Concrete Research, 35(5), 1008-1013.

[54] Cui, X., Zhang, J., Zhang, N., Gao, Z., Sui, W., & Wong, C. (2014). Improvement of permeability measurement precision of pervious concrete. *Journal of Testing and Evaluation, 43*(4), 812-819.

[55] CASTRO, RR; BENTHEM, Kv. Sintering. [electronic resource] : mechanisms of convention nanodensification and field assisted processes. Berlin ; New York : Springer, c2013., 2013. (Engineering materials: v.35). ISBN: 9783642310096.

[56] GORSHKOV, V; KUZMENKO, V; PRIVMAN, V. Mechanisms of Interparticle Bridging in Sintering of Dispersed Nanoparticles. 2014.

[57] UPADHYAYA, GS. SINTERING FUNDAMENTALS: HISTORICAL ASPECTS.

Materials Science Forum. 835, 1-49, Jan. 2016. ISSN: 16629752.

[58] INDYK, SJ; BENAROYA, H. A structural assessment of unrefined sintered lunar regolith simulant. Acta Astronautica. 140, 517-536, Nov. 1, 2017. ISSN: 0094-5765

[59] Shi, J. (1999). Thermodynamics and Densification Kinetics in Solid-state Sintering of Ceramics. Journal of Materials Research, 14(4), 1398-1408. doi:10.1557/JMR.1999.0190

[60] HIRATA, Y; HARA, A; AKSAY, IA. Thermodynamics of densification of powder compact. Ceramics International. 35, 2667-2674, Jan. 1, 2009. ISSN: 0272-8842.

[61] Gualtieri, T., & Bandyopadhyay, A. (2015). Compressive deformation of porous lunar regolith. Materials Letters, 143, 276-278.

[62] Lunar Sample Preliminary Examination Team (1). (1969). Preliminary examination of lunar samples from Apollo 11. Science, 1211-1227.

[63] McKay, D. S., Heiken, G. H., Taylor, R. M., Clanton, U. S., Morrison, D. A., & Ladle, G. H. (1972). Apollo 14 soils: Size distribution and particle types. In Lunar and Planetary Science Conference Proceedings (Vol. 3, p. 983).

[64] Charette, M. P., McCord, T. B., Pieters, C., & Adams, J. B. (1974). Application of remote spectral reflectance measurements to lunar geology classification and determination of titanium content of lunar soils. Journal of Geophysical Research, 79(11), 1605-1613.

[65] Seal, S., Reid, D., & Hench, L. (2013). U.S. Patent No. US8404609B2. Washington, DC: U.S. Patent and Trademark Office.

[66] Júnior, M., Bezerra, H. D. J. C. L., Politi, F. S., & Paiva, A. E. M. (2014). Increasing the compressive strength of Portland cement concrete using flat glass powder. Materials Research, 17, 45-50.

[67] Ravina, D., & Mehta, P. K. (1988). Compressive strength of low cement/high fly ash concrete. Cement and Concrete research, 18(4), 571-583.

[68] Shuai Li, Paul G. Lucey, Ralph E. Milliken, Paul O. Hayne, Elizabeth Fisher, Jean-Pierre Williams, Dana M. Hurley, and Richard C. Elphic (20 August 2018). "Direct evidence of surface exposed water ice in the lunar polar regions". Proceedings of the National Academy of Sciences of the United States of America. doi:10.1073/pnas.1802345115. Retrieved 21 August 2018.

[69] Cloutis, E., Berg, B., Mann, P., & Applin, D. (2016). Reflectance spectroscopy of low atomic weight and Na-rich minerals: Borates, hydroxides, nitrates, nitrites, and peroxides. Icarus, 264, 20-36.

[70]Ustinovshchikov, Y.I. & Sapegina, I.V. Inorg Mater (2005) 41: 24. https://doi.org/10.1007/s10789-005-0067-3

[71] Lide, David R (1992). CRC handbook of chemistry and physics: A ready-reference book of chemical and physical data. Boca Raton: CRC Press

[72] Ma, R., Fang, K., Yang, J. G., Liu, X. S., & Fang, H. Y. (2014). Grain refinement of HAZ in multi-pass welding. *Journal of Materials Processing Technology*, *214*(5), 1131-1135.

[73] Boumerzoug, Z., Derfouf, C., & Baudin, T. (2010). Effect of welding on microstructure and mechanical properties of an industrial low carbon steel. *Engineering*, *2*(07), 502.

[74] Kučerová, L., Bystrianský, M., & Jeníček, Š. (2017, February). High ductility of bainite-based microstructure of middle carbon steel 42SiMn. In *IOP Conference Series: Materials Science and Engineering* (Vol. 179, No. 1, p. 012044). IOP Publishing

[75] Schade, C., Murphy, T., Lawley, A., & Doherty, R. (2015). Microstructure and mechanical properties of a bainitic PM Steel. *Hoeganas Corporation*.F